Title
Sustained neuronal activity in human prefrontal cortex links perception and action

Author
Haller, Matar

Publication Date
2016

Peer reviewed|Thesis/dissertation

Sustained neuronal activity in human prefrontal cortex links perception and action

by

Matar Haller

A dissertation submitted in partial satisfaction of the

requirements for the degree of

Doctor of Philosophy

in

Neuroscience

in the

Graduate Division

of the

University of California, Berkeley

Committee in charge:

Professor Robert T. Knight, Chair
Professor Jonathan D. Wallis
Professor Richard B. Ivry
Professor Keith Johnson

Spring 2016

Abstract

Sustained neuronal activity in human prefrontal cortex links perception and action

by

Matar Haller

Doctor of Philosophy in Neuroscience

University of California, Berkeley

Professor Robert T. Knight, Chair

The prefrontal cortex (PFC) is critical for organizing thought and behavior in accordance with internal goals. Patients with prefrontal lesions do not exhibit easily observable sensory deficits or simple behavioral deficits, but instead are unable to select appropriate responses based on internal representations. Neuroimaging in humans and single unit studies in non-human primates show PFC involvement across many task contexts requiring higher order control of behavior. However, despite converging evidence from neuroimaging and electrophysiology, the neuronal mechanism of flexible thought and behavior remains one of the most fundamental and elusive questions in neuroscience. One hypothesis posits that the PFC functionally bridges stimulus evaluation and response execution across time and cortical space, yet how this region implements the stimulus-to-response transformation is unknown. The first study described here defines how response selection is implemented during goal-directed behavior by examining the timing, magnitude, and spatial distribution of local cortical activation in humans. These results demonstrate that intrinsically sustained stimulus-to-response activation provides the foundation for binding stimulus processing with response execution on a single trial basis. Notably, this effect is seen across multiple tasks and sensory modalities. The second study introduces a novel method for probing how oscillations contribute to cognitive control by algorithmically extracting the center frequencies and bandwidths of oscillatory components in electrophysiological power spectra. The results demonstrate that the use of individualized frequency bands, which account for oscillatory heterogeneity, unmasks relationships between task and behavior that are hidden when using predefined, canonical frequency bands. Oscillatory dynamics support neuronal communication, and as such the method presented here is a critical step in understanding how the PFC exerts cognitive control over distributed cortical and subcortical regions supporting goal-directed behavior.

Table of Contents

Acknowledgements **iii**

1. Introduction **1**

1.1 Background 1

1.2 Lateral PFC anatomical organization and connectivity 1

1.3 Neuropsychology – PFC lesion studies 2

1.4 Electrophysiology and neuroimaging 4

1.5 Outline 9

2. Sustained neuronal activity in human prefrontal cortex links perception and action **10**

2.1 Introduction 11

2.2 Methods 13

2.3 Results 23

2.4 Discussion 35

3. Algorithmic identification of oscillatory frequency and bandwidth **41**

3.1 Introduction 42

3.2 Methods 43

3.3 Results 50

3.4 Discussion 56

4. Concluding Remarks **59**

5. References **61**

Dedicated to my grandparents, for giving me tenacity.

Acknowledgements

This dissertation represents the culmination of one of the more intense, challenging, and rewarding periods I have experienced. I could not have persisted without the support of my parents, brother, and husband, who knew when to give advice and when to just listen, and who never doubted that I would succeed, even when I was less than certain. I am especially grateful to Liran, my best friend and partner, who joined me on this journey. You not only made sure we savored the positive moments but also pushed me through the difficult stretches. After almost six years, two weddings, and one adorable baby, we are wrapping up this chapter and moving on to the next. I am ready and excited for our next adventure together. I love you.

Thank you to my friends and colleagues. This experience would have been empty without you, without the dinners, chai dates, hikes, advice, and deep conversations. Thank you also to Bradley Voytek, for always being willing to share ideas and collaborate. I would especially like to thank Avgusta Shestyuk for gracefully balancing the roles of mentor and friend.

I would like to extend my deepest appreciation and gratitude to my advisor, Robert Knight, whose support, guidance, and generosity ensured my success. You inspired me as an undergraduate, pushed me to succeed as a graduate student, and now, after a decade of working together, are letting me loose. Thank you.

Importantly, none of this work would have been possible with the generosity and bravery of the patients who consented to participate in this research.

The studies in this dissertation were supported in part by a National Science Foundation Graduate Research Fellowship DGE1106400.

Chapter 1

Introduction

1.1 Background

Nearly 150 years ago, David Ferrier concluded that prefrontal cortex lesions in monkeys were "not followed by any definite physiological result", yet they instead caused "a very decided alteration in the animal's character and behavior… while not actually deprived of intelligence, they had lost, to all appearance, the faculty of the attentive and intelligence observation" (Ferrier, 1878). A century later, Alexander Luria declared that the frontal lobes "are in fact a superstructure above all other parts of the cerebral cortex, so that they perform a far more universal function of general regulation of behavior than that performed by the posterior associative center" (Luria, 1973).

Situated anterior to the precentral gyrus and to premotor cortex, prefrontal cortex (PFC) is fundamental to cognition and behavior, enabling humans to flexibly respond to ever-changing environmental demands. Anatomically, the PFC can be defined as the region receiving projections from the mediodorsal nucleus of the thalamus (Fuster, 2015). Disproportionately large in humans, PFC encompasses nearly one third of the neocortex (Preuss, 2011). It is ideally situated for coordinating neuronal processing and integrating information, with connections to nearly all cortical and subcortical areas (Fuster, 2015 ; Miller & Cohen, 2001). Developmentally, the PFC is the slowest region to develop of all brain regions, reaching maturity in humans only in early adulthood (Diamond, 2002). The PFC in humans can be grossly subdivided into: 1) Lateral prefrontal cortex (LPFC), 2) Orbitofrontal (OFC), and 3) Medial PFC. This thesis will focus on the lateral prefrontal cortex.

1.2 Lateral PFC anatomical organization and connectivity

The lateral PFC spans the region adjacent to premotor cortex (Brodmann area 6; BA) to the frontal pole (BA 10). The LPFC can be further subdivided into dorsolateral, ventrolateral and rostral PFC subregions. Dorsolateral PFC contains BA 9, 46 and 9/46, as well as BA 8 (frontal eye fields). It is adjacent to premotor cortex, covers the superior and middle frontal gyri, and extends to the frontal pole (rostral PFC; BA 10). Ventrolateral PFC lies on the inferior frontal gyrus and

consists of BA 44, 45 and 47 (Petrides, 2005). In addition to these anatomical subdivisions, lesion, neuroimaging, and electrophysiological evidence also support a functional subdivision of lateral PFC along a rostro-caudal axis, ranging from dorsal premotor cortex (BA 6/8) to the frontal pole (Badre, 2008 ; Badre & D'Esposito, 2009 ; Voytek, et al., 2015a).

The LFPC has direct and indirect connectivity with many cortical and subcortical areas, making it ideally situated for integrating information from diverse sites and influencing processing in posterior regions. The parvocellular portion of the mediodorsal nucleus of the thalamus relays information from other subcortical structures to the LPFC via subcortical afferents (Fuster, 2015). The LPFC also receives cortical afferents from multimodal association areas via multiple white matter fiber tracts. The superior longitudinal fasiculus connects the parietal lobe with the LPFC, and conveys visuospatial information to the dorsolateral PFC and higher order somatosensory input to ventrolateral PFC (Petrides & Pandya, 2002). The uncinate fasiculus conveys visual object information to ventrolateral PFC from inferotemporal cortex, while the arcuate fasiculus and extreme capsule convey auditory information from the superior temporal gyrus. The dorsolimbic pathway links the medial temporal lobe with the dorsolateral PFC, providing a pathway for memory processing. In addition to providing sensory and multimodal information to the LPFC, these fiber pathways are bidirectional, enabling the LPFC to modulate processing in posterior association cortices (Petrides, 2005).

There is also extensive reciprocal connectivity within the PFC in addition to connections with subcortical and posterior cortical regions. This local connectivity includes short U-shaped fibers linking adjacent gyri as well as intralobar fiber tracts linking distant regions within the PFC (Catani et al., 2012). This extensive connectivity between the PFC and cortical and subcortical regions as well as within the PFC ideally positions this region to modulate and influence processing across diverse brain networks.

1.3 Neuropsychology – PFC lesion studies

Much of the initial understanding of the role of LPFC came from observations of humans and nonhuman primates with damage to this region. Lesion evidence suggests that damage to dorsolateral PFC results in multiple cognitive deficits in attention, working memory, planning, rule learning and motivation (Szczepanski & Knight, 2014).

Patients with dorsolateral PFC damage exhibit problems with allocating attention and are distractible. In an auditory delayed-match-to-sample task, patients with dorsolateral PFC damage were impaired by the presence of distractors during the delay and exhibited enhanced primary auditory event related potentials (ERPs) to distracting sounds, suggesting that the dorsolateral PFC acts as an inhibitory

gating mechanism for distracting information (Chao & Knight, 1998). Other studies have found that patients with unilateral dorsolateral PFC damage exhibit decreased contralateral extrastriate neuronal responses (Barceló, Suwazono, & Knight, 2000 ; Voytek, et al., 2010b), suggesting that the dorsolateral PFC can also support attention by facilitating processing in posterior cortical areas.

In addition to problems allocating attention, lesions to dorsolateral PFC also result in working memory deficits. These are manifest as problems in monitoring and manipulating representations in working memory but with intact maintenance and rehearsal, likely because of compensation by the intact hemisphere (Barbey, Koenigs, & Grafman, 2013 ; D'Esposito, Cooney, Gazzaley, Gibbs, & Postle, 2006). Patients with dorsolateral PFC damage are also impaired in source memory and temporal ordering of learned events, suggesting that the dorsolateral PFC is important for linking facts to context (Szczepanski & Knight, 2014). Patients with dorsolateral PFC damage also do not exhibit memory facilitation for novel stimuli, probably due to lack of preferential attention to novel stimuli (Daffner et al., 2000 ; Kishiyama, Yonelinas, & Knight, 2009 ; Knight, 1984). In addition, patients with dorsolateral PFC damage often exhibit "goal neglect"; they disregard task requirements, although they know and remember them (Duncan et al., 2008), suggesting this region is central to planning and maintaining sequences of actions and goals.

Patients with lesions to ventrolateral PFC exhibit problems with allocating spatial attention, language processing, and response inhibition (Szczepanski & Knight, 2014). Right-handed individuals with damage to the right inferior frontal gyrus (IFG) or right frontal eye-field exhibit symptoms of visiospatial neglect, failing to orient and attend to the contralesional side of space. Damage to the right IFG also affects response inhibition during motor control tasks. One theory posits that the right IFG acts as a brake over response tendencies (Aron, Robbins, & Poldrack, 2014). For example, during a Stop-Signal task, patients with right IFG lesions were slower to initiate stops than controls, and their lesion volume predicted stop initiation time (Aron, Fletcher, Bullmore, Sahakian, & Robbins, 2003). However, there is also evidence of unimpaired stop-signal performance in lateral PFC patients, with no correlation between extent of right IFG damage and reaction time (Krämer et al., 2013). Instead, patients committed more errors and had more variable reaction times in both Go/Nogo and Stop-Signal tasks, suggesting a role for PFC in action restraint but not actual action cancellation. In contrast, the left IFG (Broca's area BA 44/45) is part of a hemispheric language production, comprehension and monitoring network (Riès, Xie, Haaland, Dronkers, & Knight, 2013 ; Toga & Thompson, 2003). Damage to this network results in nonfluent aphasia, in which patients exhibit word-finding impairments, speak in short phrases with simple syntactic structure, and omit grammatical markers and function words (Szczepanski & Knight, 2014).

In addition to the anatomical subdivision discussed above, lesion evidence suggests that the PFC is functionally organized along a rostro-caudal axis, such that posterior to anterior PFC progressively mediates more abstract, higher-order control (Azuar et al., 2014 ; Badre, Hoffman, Cooney, & D'Esposito, 2009). In a decision-making task requiring actions at different degrees of rule abstraction, PFC damage impaired actions at a level of abstraction based on lesion location. This suggests that rostral PFC engages when task demands are abstract, while caudal PFC independently controls simple sensorimotor transformations when higher order control is not required.

1.4 Electrophysiology and neuroimaging

Lesion studies are essential to providing a causal link between the PFC and higher order cognitive function. However, the brain is composed of multiple interacting networks that engage in a task specific manner, and there is not always a direct mapping between the deficit that occurs with damage to a region and the role of that region. Electrophysiology and neuroimaging research have complemented and extended lesions studies by revealing the mechanisms underlying the role of the PFC in influencing and regulating cognition and behavior.

Decades of single and multi unit studies in nonhuman primates have enabled researchers to identify neuronal correlates of a wide range of cognitive control cognitive processes in PFC. Individual neurons in monkey PFC can encode abstract rules that are not explicitly tied to particular stimuli (Wallis, Anderson, & Miller, 2001). In addition to encoding novel and abstract stimulus-response mappings, PFC neurons exhibit plasticity and adapt their response properties to encode information relevant for the current task (Cromer, Roy, & Miller, 2010 ; Freedman & Assad, 2006 ; Roy, Riesenhuber, Poggio, & Miller, 2010). There is evidence that PFC neurons also act as a gateway for task information along the sensorimotor pathway. During a flexible visuomotor categorization task, neurons in higher sensory cortex (inferior temporal and V4) were first to encode task information. Following this transient encoding burst, neurons in PFC and lateral intraparietal area (LIP) represented sustained task information before it spread to other cortical regions (Siegel, Buschman, & Miller, 2015), suggesting that PFC modulates task information before it reaches response circuitry.

Cortical recordings from nonhuman primates have been essential to furthering our understanding of PFC function. However, nonhuman primate recordings are limited in their ability to inform about naturalistic behaviors that go beyond learned stimulus-response contingencies. Monkeys are over-trained and are experts in the experimental task, often performing at nearly 90% accuracy before recording begins. Yet the PFC is critical for situations where the stimulus-response mapping is ill defined or changing (Miller & Cohen, 2001). This fundamental PFC role can best be studied in human subjects, who are able to perform complex tasks without

requiring extensive training in a specific experimental paradigm. Electroencephalography (EEG), magnetoencephalography (MEG), and functional magnetic resonance imaging (fMRI) are noninvasive methods used to study PFC processing in humans.

EEG and MEG have millisecond temporal resolution, measuring neuronal activity as it unfolds. However, both EEG and MEG have a number of limitations (Cohen & Halgren, 2009 ; Lachaux, Axmacher, Mormann, Halgren, & Crone, 2012 ; Luck, 2014 ; Nunez & Srinivasan, 2006). Measured at the scalp, both EEG and MEG measure activity from postsynaptic currents in pyramidal cells mainly in cortical layers III and V. However, the current as measured at the scalp may be generated by an infinite number of underlying generators, idealized as dipoles (the "inverse problem"). Solving the inverse problem requires a number of assumptions, and source localization for these two methods is problematic. This problem is somewhat alleviated by the use of lesion studies, which can provide important insights into the role of PFC in regulating EEG and MEG signals (see **Neuropsychology** above). However, even in lesion studies the current sources for intact regions can only be inferred. Further complicating matters, the magnetic fields of radially oriented dipoles cancel, so MEG is only sensitive to tangentially oriented dipoles, largely located in the sulci. Meanwhile, current flow measured with EEG is dominated by radially oriented dipoles located on gyri close to the skull. In addition, spectral power is inversely proportional to frequency ($1/f$ power law scaling) and decreases with distance from the cortical surface. This means that the EEG signal is largely insensitive to local cortical activation reflected in high frequency power. The skull also acts as a low-pass filter, which results in spatial smearing of the EEG signal and further amplitude attenuation. Finally, due to signal-to-noise constraints, both methods rely on averaging of activity over multiple trials with respect to a repeated event to produce a reliable signal and can miss trial-by-trial dynamics.

With broad anatomical coverage and better spatial localization than either EEG or MEG, fMRI has deepened our understanding of the role of lateral PFC in regulating information processing. In a perceptual decision-making task, activity in dorsolateral PFC correlated with differences between signals in sensory regions and increased proportional to the strength of the sensory signal (Heekeren, Marrett, Bandettini, & Ungerleider, 2004), suggesting that dorsolateral PFC integrates information from upstream sensory regions to compute perceptual decisions. A more recent study reported a network of brain regions that engaged across seven different tasks, all involving executive processes including attention, goal maintenance, and performance monitoring (Fedorenko, Duncan, & Kanwisher, 2013). This network of brain regions included the dorsolateral PFC, suggesting that this region is functionally general and engaged in a broad range of cognitive processes requiring control.

Neuroimaging also supports a role for ventrolateral PFC in cognitive control. The right ventrolateral PFC supports both attention and response inhibition processes (Aron et al., 2014 ; Bari & Robbins, 2013). An fMRI meta-analysis found that right inferior frontal junction (IFJ) is recruited by reflexive orienting tasks and supports detection of behaviorally relevant stimuli, while neighboring subregions are active during motor inhibition (Levy & Wagner, 2011). Left ventrolateral PFC also exhibits functional heterogeneity, with studies identifying both language-selective and memory control regions within IFG (Badre & Wagner, 2007 ; Fedorenko, Duncan, & Kanwisher, 2012). Furthermore, left IFG subregions activated by diverse cognitive control tasks border language-selective subregions, suggesting a fine structure within left IFG for domain-general cognitive control and language production.

Neuroimaging converges with lesion evidence to support a rostro-caudal gradient of abstraction in lateral PFC. As the context for response selection becomes more abstract and relevant over a longer time window, progressively more anterior subregions become active, with activation moving from dorsal premotor regions to mid-dorsolateral PFC (Koechlin, Ody, & Kouneiher, 2003). In a task manipulating priming at the response, decision, and semantic levels, repetition suppression occurred in progressively anterior regions of ventrolateral PFC with increasing representational abstraction (Race, Shanker, & Wagner, 2009). Thus, there is evidence for a functional rostro-caudal gradient along both dorsolateral and ventrolateral PFC.

Although fMRI overcomes the spatial limitations inherent in EEG and MEG, it cannot track cortical dynamics as they unfold on a subsecond scale due to the time lag in neurovascular coupling (4-6 seconds). Furthermore, fMRI only indirectly measures neuronal function through hemodynamics (blood oxygen level-dependent signal; BOLD) and cannot disentangle local cortical processing from inter-regional interactions (Hermes et al., 2011).

Direct cortical recording with subdural electrode arrays (electrocorticography; ECoG) provides an opportunity to record neuronal activity directly from human cortex and circumvents many of the issues of noninvasive methods. ECoG provides a high fidelity signal with a spectrum (DC to 200Hz) unattainable with noninvasive techniques (Buzsaki, Anastassiou, & Koch, 2012). The ECoG signal is also an order of magnitude stronger than signal obtained from scalp recordings, circumventing the high frequency signal loss compromising scalp EEG data (discussed above). Direct cortical recordings provide source localization typically at 1cm, and occasionally at 4-5mm. With its superb temporal resolution and high spatial resolution, ECoG bridges the spatial and temporal resolution gaps in noninvasive methods.

The ECoG signal contains two primary components, each carrying unique information – low frequency oscillations (<40Hz) and broadband spectral power change (Miller, Sorensen, & Ojemann, 2009). Broadband spectral power change can be observed as a change in high-frequency power (70-200Hz), and is also known as broadband high gamma (HG; (Crone, 1998 ; Miller, 2010). Local field potential power in the HG range indexes local cortical activation, and has been linked to both neuronal firing rate and to the fMRI BOLD signal (Manning, Jacobs, Fried, & Kahana, 2009 ; Mukamel et al., 2005 ; Ray & Maunsell, 2011 ; Ray, Crone, Niebur, Franaszczuk, & Hsiao, 2008).

While high frequency power reflects local information processing, low frequencies are generated by large neuronal groups and coordinate information across distant brain regions (Buzsaki & Draguhn, 2004). Oscillating neuronal groups have rhythmic fluctuations in their excitability, which constitute reoccurring temporal windows for communication and define networks. Coherent oscillations with overlapping windows of communication and a constant phase lag enable communication within a network, while the absence of coherence prevents communication and segregates networks (Fries, 2005 ; Siegel, Donner, & Engel, 2012). Cross-frequency coupling between the phase of a low frequency and the amplitude of a high frequency can provide a mechanism of local integration of interregional communication (Canolty & Knight, 2010 ; Sadeh, Szczepanski, & Knight, 2013). There is evidence that phase-amplitude coupling (PAC) between the phase of low frequency oscillations and the amplitude of HG is modulated in a behaviorally relevant manner (Canolty et al., 2006 ; Miller et al., 2010 ; Szczepanski, Crone, & Kuperman, 2014 ; Voytek, Canolty, et al., 2010a ; Voytek, Kayser, et al., 2015a), similar to the biasing of neuronal spiking activity by local field potential phase (Kayser, Montemurro, Logothetis, & Panzeri, 2009 ; Sirota et al., 2008)

ECoG studies about the role of PFC in cognitive control have extended and expanded the findings from noninvasive studies in humans and single unit studies in nonhuman primates. Broadband HG centered in dorsolateral PFC and regions of the fronto-parietal attention network is sustained throughout the duration of both top-down and bottom-up visual search (Ossandon et al., 2012). This suggests that dorsolateral PFC exerts top-down control of attention even during salient, pop-out search. This result contradicts previous fMRI studies that reported no dorsolateral PFC involvement during bottom-up visual search, perhaps because pop-out search durations are too short to elicit a detectable BOLD signal. Noninvasive neuroimaging also lacks the temporal resolution to discern the temporal sequence of activations underlying memory encoding. A recent ECoG study of subsequent memory reported that regions identified in fMRI as associated with successful memory encoding in fact invoke two distinct networks, one associated with bottom-up perceptual processing and the second reflecting top-down control, with activation

in the IFG, posterior parietal, and ventrolateral temporal cortex (Burke et al., 2014).

Analysis of low frequency oscillations in ECoG enables the investigation how networks engage in a task-dependent manner in a way that is unattainable with fMRI. For example, a recent ECoG study found that interactions between PFC, parietal, and parhippocampal regions are mediated by coupling in distinct frequency bands during spatial or temporal memory (Watrous, Tandon, Conner, Pieters, & Ekstrom, 2013). Specifically, spatial recall is supported by coherence in a 1-4 Hz frequency band, while temporal recall is supported by coherence between 7-10 Hz. Furthermore, analysis of the electrophysiological signal also enables insights into the direction of information flow between nodes in this network. In a memory task, 4-8 Hz coherence between PFC and the medial temporal lobe increased during free recall relative to a baseline condition. Granger causality analysis suggested bidirectional information flow between these two regions, but with a greater influence of medial temporal lobe oscillations on driving the coherence than PFC oscillations (Anderson, Rajagovindan, Ghacibeh, Meador, & Ding, 2010).

The spatiotemporal resolution of ECoG also enables the temporal dissociation of dorsolateral versus ventrolateral PFC in planning and stopping actions. Dorsolateral and ventrolateral PFC exhibit different temporal profiles while subjects prepare to stop action, with dorsolateral PFC activity representing task goals and ventrolateral PFC implementing action control (Swann, Tandon, Pieters, & Aron, 2013). There is also evidence for middle frontal gyrus (MFG) involvement in online action evaluation, with increased post-response HG activity in anterior MFG to unsuccessful versus successful stops in a Stop-Signal task. Notably, HG was absent for successful stops (Fonken et al., 2016). This study also reported stop-related beta activity in left PFC, in contrast to previous reports of lateralization of stop-related activity to right IFG (Aron et al., 2014).

ECoG also supports a functional subdivision of frontal cortex based on cognitive control requirements. As task demands require increasing levels of cognitive control, broadband HG in PFC is greater relative to HG in premotor regions and predicts reaction times (Voytek, et al., 2015a). Furthermore, theta-HG PAC increases for progressively anterior sites, with no PAC within motor cortices but increased PAC between PFC theta and motor cortex HG. This suggests that theta phase encoding biases local neuronal processing across frontal subregions along a rostro-caudal gradient. These ECoG studies extend the conclusions drawn from previous fMRI studies and point to a critical role for ECoG in examining the spatiotemporal profile of cognitive control in the PFC.

1.5 Outline

The first part of this thesis utilizes ECoG and leverages the temporal and spatial specificity of the HG signal to examine goal-directed behavior, specifically how stimulus perception is translated into response selection. We identify a robust domain and modality independent pattern of neuronal activation centered in PFC that predicts motor output on a trial-by-trial basis with near perfect accuracy. We suggest that this activation reflects a functional substrate for domain-general spatiotemporal integration of information, critical for flexible, goal-directed behavior. The second part of this thesis describes a novel method for algorithmically extracting the oscillatory components of electrophysiological signals on an individual basis. We validate the algorithm against synthetically generated data and then apply it to data recorded at different electrophysiological scales: local field potential recordings in nonhuman primates and scalp EEG from humans. We utilize this method to extrapolate novel relationships between oscillatory parameters and working memory. This method will enable us to examine how the PFC exerts cognitive control in a more fine-grained manner. Future planned work will use custom oscillatory components to identify PFC-centered networks and the mechanisms of PFC control.

Chapter 2

Sustained neuronal activity in human prefrontal cortex links perception and action

Abstract

How do humans flexibly respond to changing environmental demands on a sub-second temporal scale? Extensive research has highlighted the role of the prefrontal cortex in diverse cognitive processes, yet the core mechanism that translates sensory information into behavior remains undefined. Utilizing direct human cortical recordings, we investigated the temporal and spatial evolution of neuronal activity, indexed by the broadband gamma signal, while sixteen participants performed an array of cognitive tasks. Here we describe a robust domain- and modality-independent pattern of sustained stimulus-to-response neural activation that encodes stimulus features and predicts motor output on a trial-by-trial basis across all tasks with near-perfect accuracy. This sustained activation, centered in the prefrontal cortex, is required for successful response selection and provides a functional substrate for domain-general transformation of perception into action, critical for flexible behavior.

2.1 Introduction

The neural mechanism of flexible thought and behavior in humans remains one of the most fundamental and elusive questions in neuroscience. Much research has been dedicated to examining how humans and other animals process stimulus information and execute a behavioral response. Yet, how the brain binds stimulus processing with response execution remains poorly understood, exemplifying a core "black box" problem in neuroscience. Fuster and colleagues propose that neuronal spatiotemporal integration may be a potential mechanism of such stimulus-response binding (Fuster, 2002 ; Fuster, Bodner, & Kroger, 2000). Specifically, they suggest that while initial stimulus processing happens in sensory areas, the prefrontal cortex (PFC) integrates stimulus information over time, culminating in response selection. However, how the PFC implements this stimulus-to-response translation is unknown.

Profound deficits in goal maintenance, decision-making and response execution have been reported across species following PFC lesions (Fuster, 2015 ; Stuss & Knight, 2012 ; Szczepanski & Knight, 2014). Likewise, numerous neurological, psychiatric and developmental disorders are also characterized by compromised PFC functioning(Callicott et al., 2000 ; Just, Cherkassky, Keller, & Minshew, 2004 ; Mayberg, 2001), highlighting the importance of understanding the role of the PFC in human cognition. Studies in non-human primates suggest that PFC neurons coordinate activity across functionally linked brain regions through temporally and spatially distributed neuronal computation. In particular, sustained neural activation has been shown to support decision-making, working memory, and response selection in non-human primates (Hernandez, Zainos, & Romo, 2002 ; Kim & Shadlen, 1999 ; Rainer, Rao, & Miller, 1999 ; Siegel et al., 2015 ; Stokes, 2015), and has also been reported in studies utilizing direct cortical recordings in humans during visual search and verb generation (Edwards et al., 2010 ; Ossandon et al., 2012). Similarly, human neuroimaging studies have identified the PFC as the core element in a distributed network of brain regions exhibiting sustained activation during tasks requiring domain-general cognitive processing and response selection (Curtis & Lee, 2010 ; D'Esposito & Postle, 2015).

Most studies have examined sustained neural activation during experimentally constrained delay periods; however naturalistic behaviors are typically self-paced and rely on self-determined response windows. Thus, it is unknown how intrinsically sustained neuronal activation in the PFC functionally links stimulus processing with response selection and execution. Multiple key questions remain. First, the spatiotemporal evolution of intrinsically sustained activation that links sensory and motor processing during complex cognitive tasks is undefined. Second, the generalizability of sustained activation across species, tasks, modalities, and cortical regions has not been established. For example, studies in non-human primates typically rely on data obtained from well-trained animals performing

highly structured tasks, which limits the ability to inform about domain-general cognitive processing during diverse naturalistic human behavior. Finally, it is unknown whether sustained activity observed in human neuroimaging and single unit animal studies reflects a single cognitive process (e.g., memory engram representation in working memory) or whether it reflects multiple task-specific sub-processes, unfolding in the stimulus-to-response temporal window, but each with unique temporal and spatial distributions.

To examine how intrinsically sustained activation in the PFC functionally bridges stimulus evaluation and response execution in time and across cortical space, we analyzed electrocorticography (ECoG) data recorded from multiple cortical areas (1344 electrodes) in 16 participants performing eight tasks, ranging in stimulus modality, cognitive demand, and response execution requirements (**Figs. 2.1a, 2.2**). Broadband high gamma signal (HG; 70-150 Hz) was used to index local cortical activation (Crone, 1998 ; Lachaux et al., 2012 ; Miller et al., 2014). The large number of tasks encompassing varied cognitive processes, along with the superb temporal resolution and broad neuroanatomical coverage afforded by ECoG methodology, enabled us to define the neural process by which flexible response selection processing is implemented in humans during goal-directed behavior.

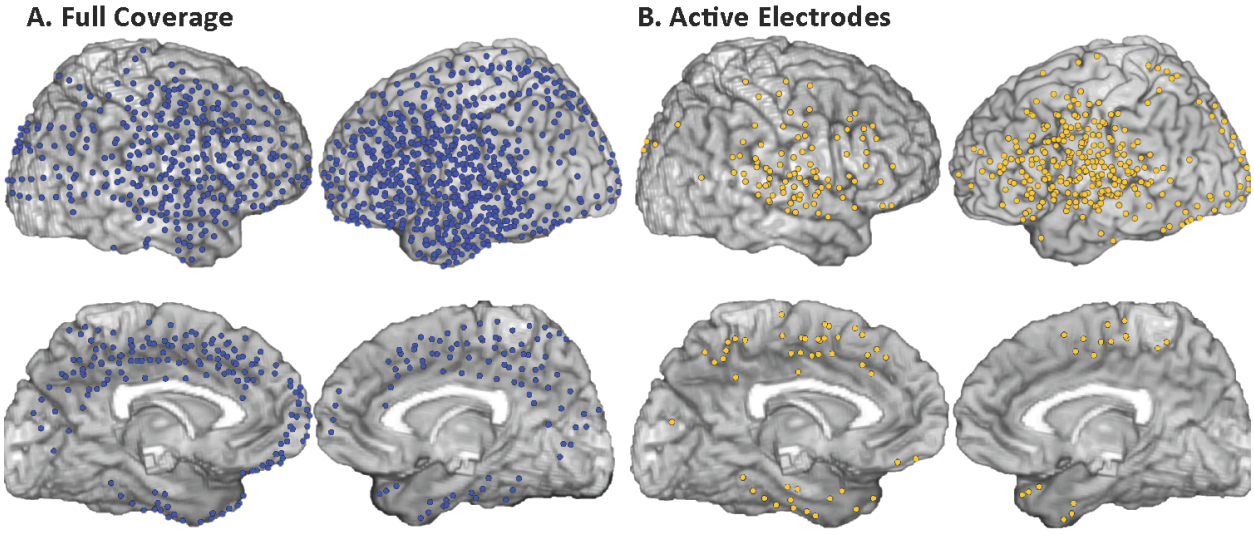

Figure 2.1 Full electrode coverage and distribution of HG activation. (**a**) Data were recorded from 1344 electrodes across 16 subjects performing between 1-6 tasks (average 2 tasks per participant). (**b**) 37% of all recorded sites exhibited a significant increase in HG activity (stimulus- or response-locked active electrodes).

2.2 Methods

Participants

Eighteen participants undergoing neurosurgical evaluation for refractory epilepsy were initially recruited. Participants were implanted with one or more subdural electrode arrays (2.3 mm exposed electrode diameter with 10 mm inter-electrode spacing) for approximately one week to determine epileptogenic focus (see **Methods** for electrode localization procedures). Electrode number and placement was dictated by clinical needs. Electrode coverage for most brain areas was represented in multiple participants (**Fig. 2.1a**), which limits the potential influence of any single pathology and enables broad generalization of results. Participants willing to participate in the study during lulls in clinical treatment provided written informed consent. All procedures were carried out in accordance with protocols approved by the Institutional Review Boards of University of California (UC) Berkeley, UC San Francisco, the Stanford School of Medicine, California Pacific Medical Center (CPMC), and the Johns Hopkins University School of Medicine. One participant was excluded due to a stroke-related cortical lesion and one participant was excluded because we were unable to obtain electrode localization information. All remaining participants had normal IQ and were fluent in English, except for one Spanish-speaking participant who completed a Spanish version of the Visual Categorization task. See **Table 2.1** for participant information.

Tasks and stimuli

Eight tasks, varying in difficulty and stimulus modality, were used. Task selection for each participant was determined by electrode location, time availability, and participant's willingness and ability to perform the task. Each participant performed 1-6 tasks (43 recording sessions, each corresponding to a single dataset used for analyses). Visual stimuli for all tasks were presented using a laptop (15.6" LCD screen) placed in front of participants at a comfortable distance (0.5-1 m). Auditory stimuli (50-60 dB HL) were presented through two speakers placed in front of participants. Onsets and offsets of stimuli were detected via an analog photodiode (visual) or the analog speaker channel (auditory). Participants made responses either by pressing the appropriate key on the laptop keyboard or by speaking into a microphone (response times were extracted from the analog microphone channel). See **Table 2.2** for task and stimulus information.

Auditory Categorization task: Participants were asked to verbally categorize gender morph utterances (the word "town") as being spoken by a female or a male speaker adopted from the Carnegie Mellon University Arctic Database (Kominek & Black, 2004) Gender morphed versions of the category prototypes were constructed at steps of 20, 40, 60, and 80% along the shortest trajectory between formant boundaries (Kawahara & Irino, 2005). Participants were presented with a visual cue (blue cross) for 600 ms, followed by an aurally presented morphed stimulus (524 ms), and were given 1500 ms to respond followed by jittered 1000 ms inter-trial interval

(ITI). Stimuli were presented randomly using E-Prime2 (Psychology Software Tools, Inc., Sharpsburg, PA).

Visual Categorization task: Participants were asked to verbally categorize morphed visual images as representing a cat or a dog. Cat and dog prototype images and morphed stimuli (20, 40, 60, and 80% morphs) were adapted from (Freedman, Riesenhuber, Poggio, & Miller, 2001). Participants were presented with a visual cue (blue cross) for 500 ms, followed by a visually presented morphed stimulus (600 ms), and were given 1500 ms to respond followed by a jittered 1000 ms ITI. Stimuli were presented randomly using E-Prime2.

Auditory Word Repetition task: Participants were asked to verbally repeat aurally presented words, which were selected from the Affective Norms for English Words (Bradley & Lang, 1999). Stimulus duration range was 295-1013 ms (mean = 645 ms, s.e.m. = 4.1), and were matched on length, emotional content (valence and arousal), and word frequency. Words were presented using MATLAB (The MathWorks, Inc., Natick, MA) in a pseudo-random order (no more than two words of the same part of speech presented in a row) with a jittered 4000 ms ITI.

Auditory Antonym Generation task: Participants were asked to verbally generate an antonym to an aurally presented word stimulus. Word stimuli and task structure were identical to those used for the Auditory Word Repetition task, but stimuli were presented in a different pseudo-randomized order. Participants always performed the Word Repetition task first, but the two tasks were never performed back-to-back in a recording session to avoid habituation effects.

Visual Face Categorization tasks: Participants were asked to categorize facial stimuli (NimStim dataset; (Tottenham et al., 2009)) either on the dimension of emotion (angry vs. neutral or sad vs. happy, presented in separate blocks) or gender (female vs. male, across the two blocks of emotional faces). Stimuli were presented using E-Prime2 in a randomized order on a white background. Each trial started with a black fixation cross (1500 ms) followed by a face stimulus (300 ms), which was replaced by a fixation cross (3000 ms), during which participants made the response. The trial was terminated after the response or timed out if no response was detected. Emotion and gender categorization blocks were presented in a counter-balanced order. Stimuli from the two blocks within each categorization condition were combined.

Auditory and Visual Self-Referential tasks: Participants were asked to verbally respond whether each aurally or visually presented word could be used to describe them ("yes" or "no" responses). Positive and negative adjectives were selected from the ANEW set and were matched on arousal, valence intensity, word length, and word frequency. Audio stimuli duration range was 305-1024 ms (mean = 690 ms, s.e.m. = 4.5 ms) and were presented using MATLAB. Visual stimuli (400 ms) were

presented using E-Prime2. In each task, stimuli were presented with a jittered 4000 ms ITI in a unique pseudo-random order with no more than two stimuli of the same valence presented sequentially. Task order was counter-balanced across participants.

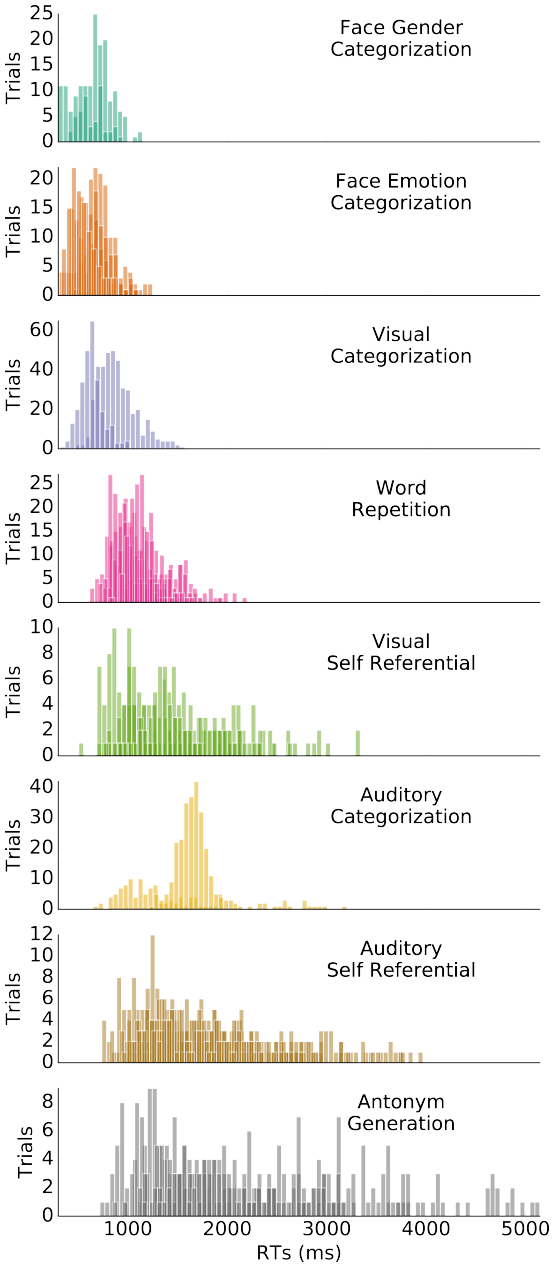

Figure 2.2 Reaction time distributions across tasks. Reaction time histogram distributions (50 ms bin spacing) are shown for each task, superimposed across participants. Face Gender Categorization N = 2, Face Emotion Categorization N = 4, Visual Categorization N = 2, Word Repetition N = 8, Visual Self Referential N = 5, Auditory Categorization N = 2, Auditory Self Referential N = 10, Antonym Generation N = 4.

Data acquisition
At UCSF and Stanford, ECoG data were acquired using a TDT recording system (Tucker-Davis Technologies, Alachua, FL), filtered online at 0.5-300 Hz and sampled at 3052 Hz (1526 Hz for one participant). At Johns Hopkins, ECoG data were recorded at 1000 Hz with a low-pass 300 Hz analog anti-aliasing filter using a 128-channel Stellate Harmonie system (Stellate Systems, Inc., Montreal, Canada). At CMPC, data were recorded at 1000 Hz using a Nihon-Kohden Neurofax EEG-1200 system (Tokyo, Japan). Analog channels (microphone, photodiode, speaker output) were recorded synchronously with ECoG signals at 24.4 kHz (UCSF, Stanford) or 1000 Hz (Johns Hopkins, CPMC). ECoG data were recorded using a subdural electrode as reference (an electrode with minimal or stable signal located away from cortical areas of interest) and a scalp electrode as ground. Sampling rates, online filters, and amplification across all recording systems were set to allow comparability across sites for the broadband gamma (70-150 Hz) signal.

Electrode Localization
A structural preoperative magnetic resonance imaging (MRI) and a post-implantation computed tomography (CT) were acquired for all participants. After confirming the MR and CT were in the lateral posterior superior orientation, the skull was stripped from the brain in the MR image. Electrode coordinates were located on the CT using Bioimage Suite (Papademetris et al., 2006). To transform the CT to brain-extracted MR space, linear and nonlinear affine and rigid registrations were run between the MR and CT. The registration best matching neurosurgeon notes and intra-operative photos was used, rendered in three dimensions and assessed for anatomical accuracy. MNI electrode localization followed similar procedures, with the brain-extracted MR registered to the MNI space. Accuracy of MNI co-registration was assessed manually for each subject by matching electrode locations to anatomical landmarks in the native MR space.

Data preprocessing
Data were recorded from 1365 ECoG electrodes. Line and equipment noise was removed using an iteratively fit zero-phase Butterworth filter. First, power spectral densities were estimated for each electrode using the multi-taper spectral estimation method from the Chronux toolbox (Bokil, Andrews, Kulkarni, Mehta, & Mitra, 2010) (tapers N = 5, time-bandwidth product W = 3). Zero-crossings in the derivative identified sharp noise peaks in the power spectrum. The filter was then iteratively fit to the noise bandwidth until the difference between the filtered and the surrounding signal was less than 0.05uV. This method ensured that each electrode was free of non-physiological noise in the specific frequencies of interest.

Data channels with poor signal quality or those located on subsequently resected tissue were excluded, leaving 1344 electrodes for further analyses. Since multiple participants completing several tasks, the total number of analyzed data channels across all datasets was 3051. Each remaining channel was down-sampled to 1000

Hz and re-referenced to a common average reference within each dataset. Data were visually inspected for periods of transient epileptiform activity or residual artifacts, which were subsequently removed from analyses.

Spectral decomposition

The analytic amplitude of the broadband high gamma signal (HG) was extracted from the raw ECoG data across the full duration of each recording session. First, a two-way, zero phase-lag, finite impulse response filter (eegfilt.m function, EEGlab toolbox (Delorme & Makeig, 2004)) was applied to extract signal in the 70-150 Hz range. This bandwidth was selected as it excludes any residual line noise and captures most of the HG power (Crone, 1998 ; Lachaux et al., 2012 ; Miller et al., 2014). Analytic amplitude was calculated by taking the absolute value of the Hilbert transform of the filtered signal. This method is comparable to other filtering techniques (e.g., wavelets; (Bruns, 2004)).

Task-active channel selection

Following spectral decomposition, HG signals were smoothed with a 10 Hz low-pass Butterworth filter and were segmented, with each trial starting 500 ms before stimulus onset and lasting until 500 ms past the maximum RT for that dataset. To assess response-related activity, trials were segmented from 500 ms before RT to 500 ms post-RT. HG signals were z-score normalized within each trial relative to the 500 ms pre-stimulus baseline (for the Visual and Auditory Categorization tasks, the baseline was taken before the cue). Trials overlapping with artifact epochs or having RTs longer than three standard deviations from the task mean were excluded. Trials on which participants did not respond, made an error, or responded with hesitation (producing pre-response vocalizations) were also excluded. No-response trials in the Antonym Generation task were analyzed separately. Data quality was confirmed through visual inspection of averaged event-related spectral perturbation (ERSP) and single-trial images, and channels with residual artifacts were removed. To identify task-active channels within each dataset, z-score normalized HG signal was subjected to a 1-sample t-test performed across trials for each time point. *P*-values were corrected for multiple comparisons (number of time points) using the False Discovery Rate correction (FDR; $q = 0.05$; (Benjamini & Hochberg, 1995)). Channels were considered task-active if they contained at least one 100 ms segment of contiguous significant FDR-corrected values with 10% signal change from baseline.

Channel clustering based on temporal morphology of the HG signal

To identify channels with common temporal patterns of HG activation, Principal Component Analysis (PCA) and hierarchical clustering were used. Each dataset was analyzed separately. PCA (correlation matrix, varimax rotation) was conducted on stimulus-locked HG time series, averaged across trials for each active channel, treating channels as features and time-points as observations. The number of significant PCs was determined using a variant of parallel analysis, whereby

comparison data were generated for increasing numbers of components until the observed eigenvalues failed to show significant improvement (Ruscio & Roche, 2012). Channels were clustered based on their principal component (PC) weights. Hierarchical clustering on a correlation distance matrix was used to identify clusters by minimizing the maximum distance between observations. In order to partition the tree into electrode groups during hierarchical clustering, the inconsistency coefficient, which compares the height of a link with the average height of links below it, was calculated for each link of the hierarchical cluster tree. Inconsistent links indicate a natural division in the data, so the median inconsistency coefficient of the tree was used as the threshold to partition the data into electrode groups. Stimulus- and response-locked cluster-wide HG activation was determined by averaging HG signal across all channels within each cluster. Clusters with low signal-to-noise ratio (<15% signal change from baseline for at least 100 ms) were excluded from further analyses. Remaining clusters were classified based on the temporal pattern of HG activity.

Cluster classification based on temporal patterns of HG activity

To identify clusters with Sustained Stimulus-to-Response HG activation, a binary 0/1 design matrix (trials x time points) was constructed, with 1s corresponding to each time point from HG onset, calculated for that cluster, through the RT for each trial. To account for potential variability in HG offsets relative to response, a dictionary of design matrices was constructed for each cluster by creating multiple versions of the original design matrix with offsets shifted from 300 ms pre-response to 450 ms post-response in 25 ms steps. Each entry in the design matrix dictionary was correlated (using Pearson's correlation) with the HG time series for that cluster. To avoid spurious significant results, non-parametric surrogate distributions (N = 10,000 achieved by randomly time-shifting HG data series relative to the design matrix entries) and an effect size threshold (R >0.1) were used to determine significance level for each correlation coefficient. Clusters with Sustained Stimulus-to-Response HG activation were defined as those with a significant above-threshold correlation for any design matrix in the dictionary given the following conditions: to ensure that HG activity was not driven primarily by response execution, the HG amplitude peak had to occur no later than 50 ms pre-response in the response-locked trace or 150 ms pre-response in the stimulus-locked trace.

Clusters that did not pass the correlation threshold were classified as Sensory if transient HG increases were present both post-stimulus and post-response for auditory tasks, or if HG increases were time-locked to stimulus onset and stimulus offset for visual tasks. Stimulus Evaluation clusters were classified as such if they exhibited transient stimulus-locked activity, with HG activation offset occurring at least 300 ms pre-response. Clusters exhibiting response-locked activity peaking 50 ms prior to response or later were classified as Response. Cluster classification was not possible for five datasets due to insufficient RT ranges to discriminate among

different types of HG activation (<100 ms min-to-max spread; see **Fig. 2.9** for temporal overlap between activation types at short RTs). These datasets were excluded from further analyses, leaving 38 usable datasets (**Table 2.2**).

For each cluster and each active channel, activation windows were defined using the onset and offset of significant HG increases (stimulus- or response-locked), smoothing over gaps in activation less than 100 ms. For sustained stimulus-to-response clusters and channels, activation windows for each trial were defined from stimulus-timed HG onset to response-timed HG offset. For subsequent analyses, distributions of HG latencies (onset, offset, peak) and amplitudes (peak and mean) were tested for normality. When normality was confirmed, differences between conditions were tested with 2-sample, 2-tailed t-tests. When normality was compromised, non-parametric tests (Kruskal-Wallis test or Mann-Whitney U test) were employed.

Behavioral relevance of HG signal parameters across datasets

HG parameters (onset, offset, and amplitude peak latency) were calculated on mean stimulus-locked data traces based on activation windows and were then averaged across all channels (by activation type) within each dataset. HG peak amplitude for Sensory and Stimulus Evaluation channels was calculated as the maximum HG value within the activation window. To avoid biased latency estimation for the Sustained Stimulus-to-Response and Response channels (due to RT-dependent activation window length), HG peak amplitude and latency for these channels were calculated using a window from stimulus onset through 500 ms past the latest response within each dataset. To assess whether time-to-response across datasets was linked to latency parameters of HG activity within each activation pattern, HG onset and peak latency values were correlated with median RTs using Pearson's correlation.

Behavioral relevance of HG signal parameters across trials

Given that RT variability (**Fig. 2.2**) may affect within-dataset HG parameters, we implemented an RT-based bin analysis across trials, subjects, and tasks. First, for each HG activation pattern, all trials across all datasets were pooled together and sorted by RT. Bins were constructed in steps of 50 ms from the minimum RT, and all trials within each bin were averaged together. Bins with low signal-to-noise ratio (<100 Sustained Stimulus-to-Response trials or <50 trials in other categories) were discarded. Thirty RT bins common across all HG activity patterns were included in further analyses. Activation windows were determined for each bin based on onsets and offsets of significant HG increases (1-sample t-test, FDR corrected). Since sustained stimulus-to-response activity was characterized by a plateau rather than a distinct peak (see **Fig. 2.8a**), additional parameters of the first plateau peak, last plateau peak, and the crossover point (the time at which the Sustained Stimulus-to-Response and Response traces intersected in each bin) were identified. Although both the Sustained and Response activity patterns were defined by their temporal

relation to the RT, the crossover point was an independent measure not derived from RT information.

To evaluate the relative contributions of different parameters of the HG signal to behavior, we conducted three separate stepwise regressions. The first regression assessed the contribution of temporal parameters of the HG signal to RTs across bins. The following predictors and their interactions were entered in the regression: HG onset, offset, and peak latency for Sensory and Stimulus Evaluation activity, as well as the latency of the first peak and the crossover point for Sustained Stimulus-to-Response activation. The second regression related stimulus offset and temporal parameters (HG onset, offset, and peak latency) of Sensory and Stimulus Evaluation activity to the latency of the first peak of Sustained Stimulus-to-Response activation. The final regression related HG amplitude parameters to normalized RTs. The following parameters were entered as predictors: HG peak amplitude values for Sensory, Stimulus Evaluation and Response activity patterns as well as mean HG amplitude values for Sustained Stimulus-to-Response activity calculated from the first plateau peak to the crossover point.

Modulation of Sustained HG activity by cognitive load

To determine the effect of cognitive load on the temporal and spatial distribution of Sustained Stimulus-to-Response activity, data were examined from participants who completed both the Antonym Generation and Word Repetition tasks, which utilize identical stimuli but differ on cognitive load. Sites with sustained stimulus-to-response activity during both tasks were classified as *overlap* sites, while sites that were active only in one of the tasks were classified as *unique*. HG onsets were averaged across sites in each task and grouping. Mann-Whitney U tests were performed to compare HG onsets between *overlap* sites in Word Repetition and Antonym Generation tasks and between *overlap* and *unique* sites in the Antonym Generation task. Since participant S15 only had 3 *overlap* sites, onsets for these sites were pooled together from both tasks for comparison across *overlap* and *unique* sites (there were no significant differences between onsets for *overlap* sites in the two tasks for this or other participants).

Stimulus feature representation indexed by HG activity

To determine whether stimulus features are represented by the HG signal, we compared HG amplitudes across different stimulus conditions for the Visual and Auditory Categorization (100/80% morphs vs. 0/20% morphs) and Antonym Generation tasks (nouns vs. adjectives). For each channel, HG amplitudes were subjected to a 2-sample 2-tailed t-test between conditions at every time point across trials. Channels exhibiting significant condition differences ($p<0.01$ for at least 100 ms) were considered sensitive to stimulus features.

HG Activity during trials with no response

To determine the role of Sustained Stimulus-to-Response activity in successful response generation, HG activity for trials on which participants failed to respond was examined in the Antonym Generation task – the only task that produced enough no-response trials. All no-response trials were pooled together and averaged across channels within each HG activation pattern. For comparison, a matching number of correct trials with longest RTs were selected for each participant to account for the duration of response selection. A 2-sample, 2-tailed t-test with FDR correction was performed on each data point comparing no-response and correct trials. A 1-sample, 2 tailed t-test with FDR correction was performed on each data point for Response traces to determine whether there were significant HG increases during no-response trials.

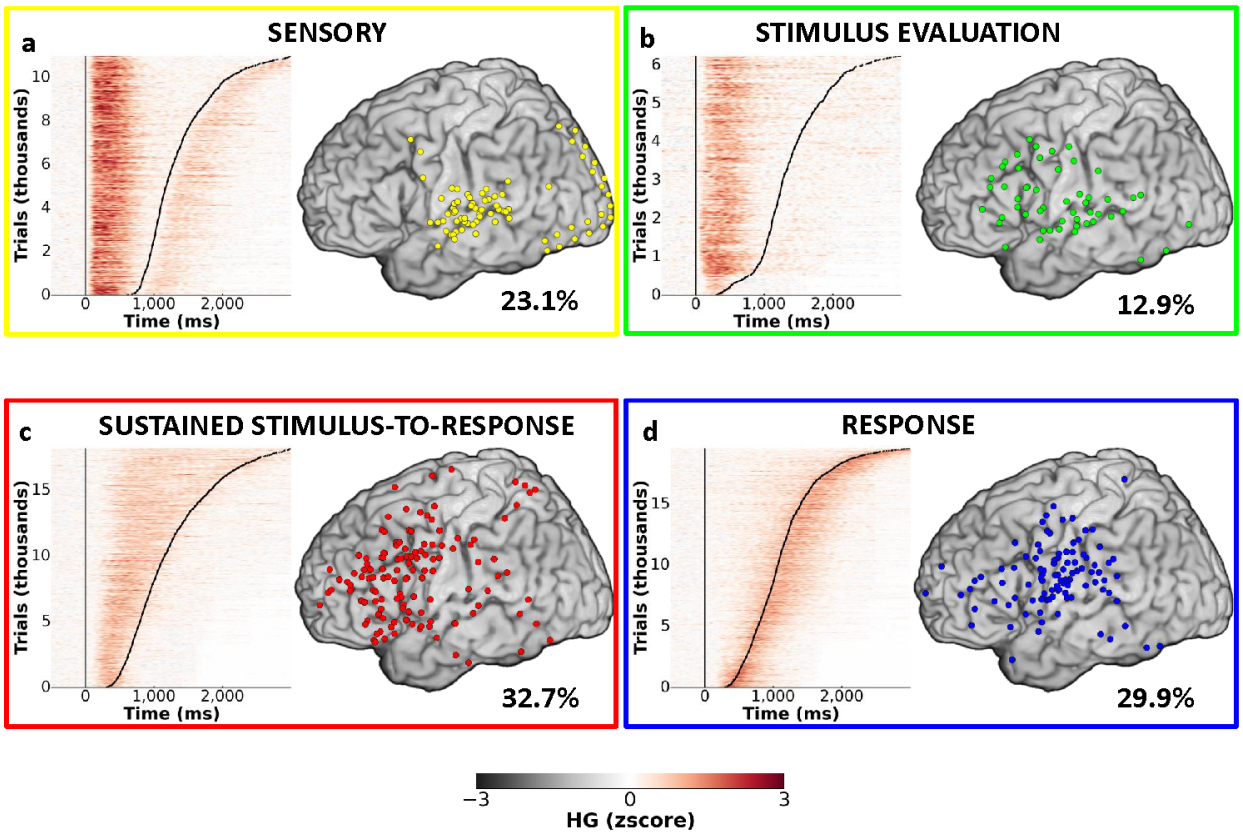

Figure 2.3 Cortical distribution and temporal dynamics of HG activation. Four patterns of HG activation were observed: Sensory (**a**), Stimulus Evaluation (**b**), Sustained Stimulus-to-Response (**c**), and Response (**d**). Single trial plots across all subjects, tasks, and channels sorted by response time (black curve) are presented on the left side of each panel. Cortical distribution (left lateral surface) of sites corresponding to each HG pattern is presented on the right. Percent of all classified electrodes exhibiting the corresponding HG pattern is indicated for each activation type.

Functional Network Analysis

To identify sites sharing common patterns of activation across trials, mean HG amplitude values within the activation window for each trial (observations) were entered into PCA analysis (using the correlation matrix without rotation) performed across all channels (features) within each dataset. PCs with eigenvalues above one (Kaiser criterion; (Kaiser, 1960)) were retained. To define functional networks based on shared trial-by-trial variability, sites with high loadings on each significant PC were identified using a threshold calculated as the smallest maximum absolute component loading value for a given dataset.

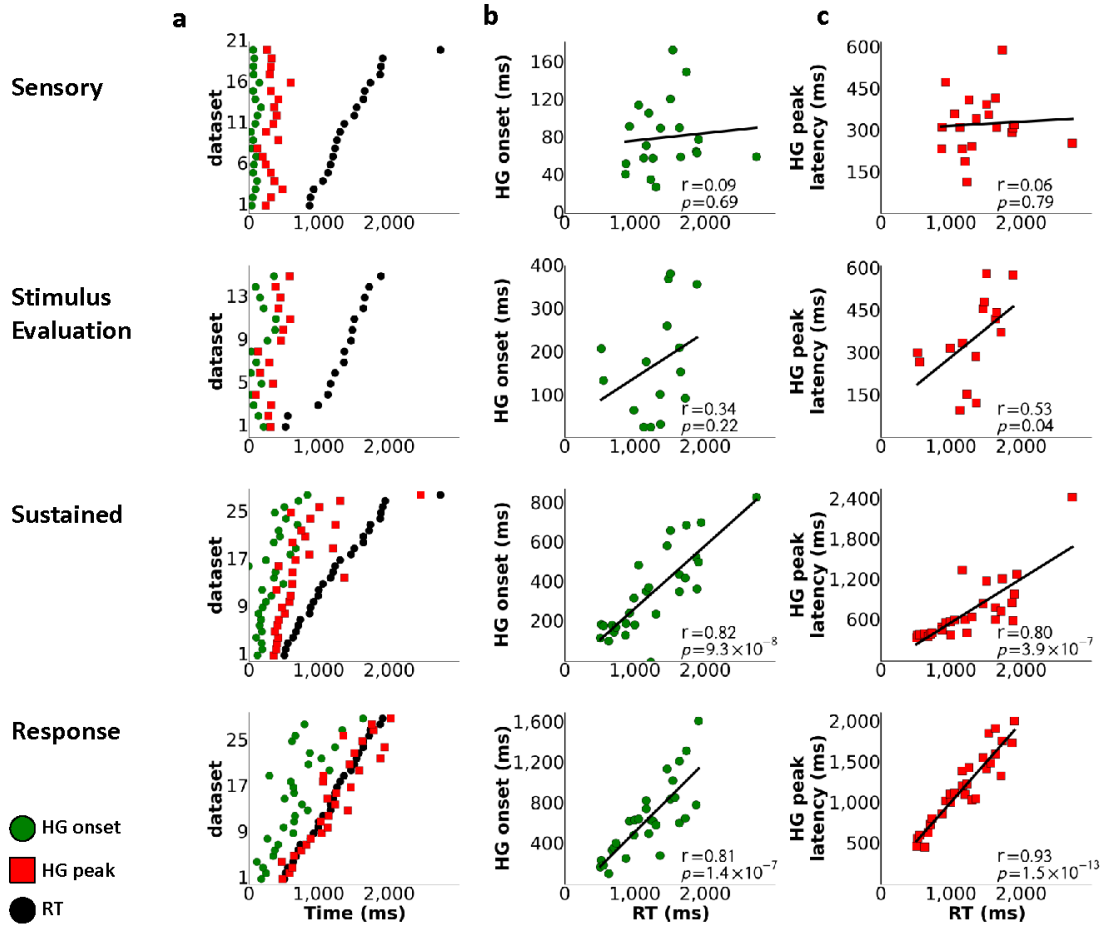

Figure 2.4 Onset and peak latency of sustained stimulus-to-response HG activity predict reaction times across datasets. (**a**) The relationship of HG onsets and peak latencies to reaction times across datasets (sorted by RT) varied as a function of activation pattern. (**b**) Correlation between reaction times and HG onset times across datasets for each pattern of HG activity. (**c**) Correlation between reaction times and HG peak latency across datasets for each pattern of HG activity. Number of datasets (tasks x subjects) for Sensory N = 20, Stimulus Evaluation N = 15, Sustained Stimulus-to-Response N = 28, Response N = 29.

2.3 Results

Time course and cortical distribution of HG activity across tasks
Task-related increases in HG activity were observed in 37% of analyzed channels (**Fig. 2.1**). To examine information processing flow from stimulus perception to response execution and to identify common patterns of HG activity across tasks, Principal Component Analysis (PCA) followed by hierarchical clustering of component scores was performed on average HG traces within each dataset, yielding 151 clusters. Four distinct temporal patterns of activation emerged, with HG onsets and peak latencies reflecting chronology of information flow (see **Methods**; **Figs. 2.3, 2.42a, 2.5 and 2.6**):

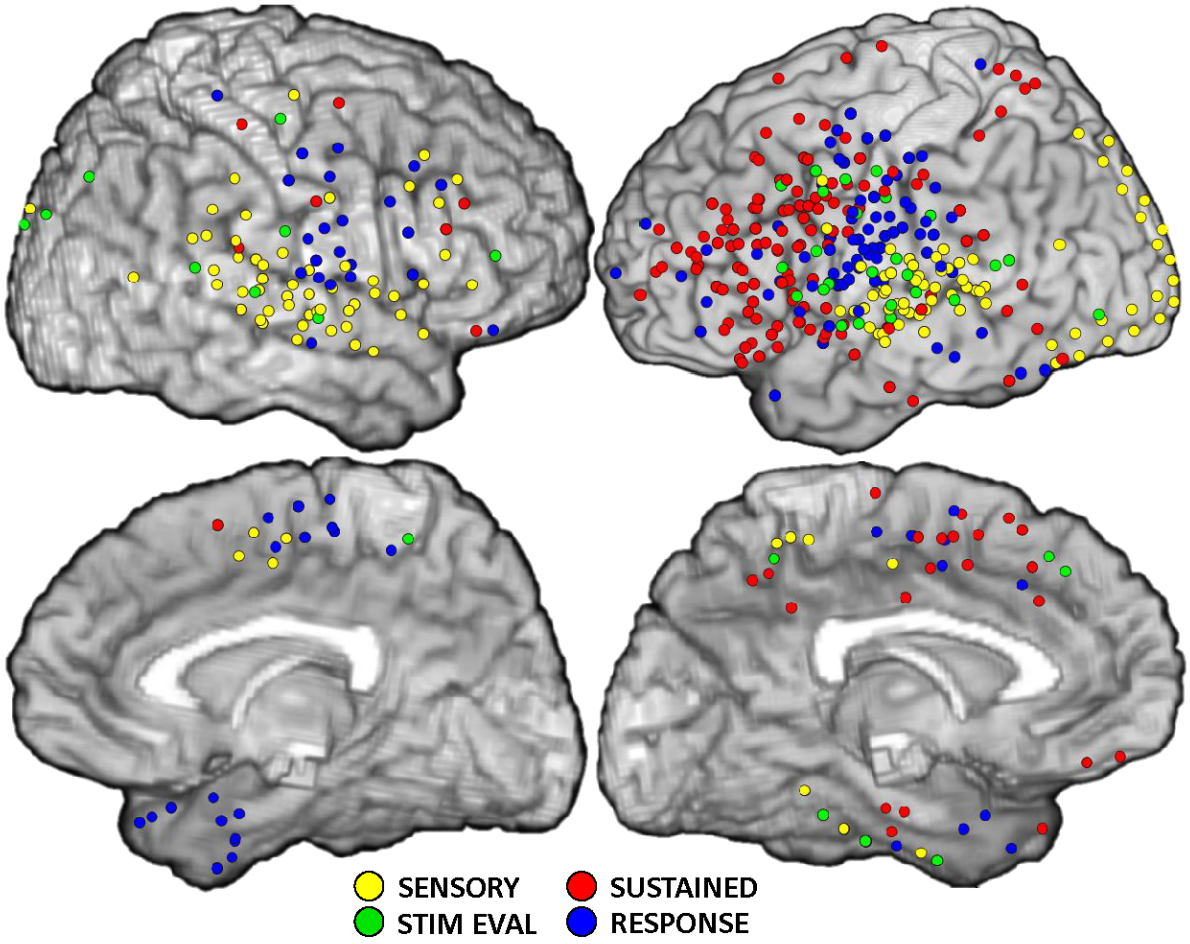

Figure 2.5 Full cortical distribution of HG activation. Cortical distribution for the Sensory, Stimulus Evaluation, Sustained Stimulus-to-Response, and Response temporal patterns of HG activity. Most active electrodes (81.9%), including Sustained Stimulus-to-Response (73.8%), were located over the left hemisphere, likely due to the linguistic nature of the tasks.

Sensory: 23.1% of active sites exhibited transient HG activity time-locked to stimulus presentation. Sensory sites were present in modality-specific regions - superior temporal gyrus (STG) for auditory stimuli and verbal responses, as well as occipital cortices for visual stimuli (**Fig. 2.3a, Fig. 2.5** for full coverage).

Stimulus Evaluation: 12.9% of active sites exhibited HG activity time-locked to stimulus presentation, but lagging in HG onsets relative to sensory activity (Mann-Whitney $U = 80.0$, $n_1 = 20$, $n_2 = 15$, $p = .01$; **Fig. 2.6**), indicating a later stage of post-sensory stimulus processing. Stimulus evaluation sites were predominantly located in auditory and visual association cortices and the PFC (**Fig. 2.3b, Fig. 2.5**).

Response Processing: 29.9% of active electrodes exhibited HG activity time-locked to response onset. The onset of the response activity preceded RTs by 351 ms (s.e.m. = 10 ms) but peaked at or immediately after the response (**Fig. 2.6**). Response sites were predominantly located around the central sulcus (on the pre- and post-central gyri) as well as on the inferior frontal gyrus (IFG) and inferior parietal lobule (IPL; **Fig. 2.3d, Fig. 2.5**).

Sustained Stimulus-to-Response Activation: The majority of active sites (32.7%) exhibited sustained stimulus-to-response activation, time-locked to stimulus presentation (mean HG onset = 350 ms post stimulus onset, s.e.m. = 40 ms) and lasting until the response (mean HG offset = 129 ms post response onset, s.e.m. = 26 ms). The onset and peak latency of the sustained stimulus-to-response activity were later than those for stimulus evaluation (for HG onsets, $U = 107.0$, $n_1 = 15$, $n_2 = 28$, $p = .005$; for HG peak latency, $U = 61.0$, $p = .0001$), but preceded response activity (for HG onsets, $U = 194.0$, $n_1 = 28$, $n_2 = 29$, $p = .0004$; for HG peak latency, $U = 61.0$, $p = .0001$; **Fig. 2.6**). Sites with sustained HG activity were located primarily in the PFC (61.6% of all sustained stimulus-to-response sites), as well as on the precentral gyrus (14.2%) and secondary association cortices (17.1%; **Fig. 2.3c, Fig. 2.5**). While the majority of active PFC sites (62.2%) exhibited sustained stimulus-to-response activation, the PFC also contained intermingled sites with stimulus evaluation (12.2%) and response (18.5%) activity.

Each processing stage engaged and peaked later than its predecessor (Kruskal-Wallis test; HG onset: $H(3) = 53.07$, $p = 1.77 \times 10^{-11}$, HG peak latency: $H(3) = 58.93$, $p = 9.95 \times 10^{-13}$), indicating the overall flow of information from sensory processing to stimulus evaluation, sustained stimulus-to-response, and culminating in response preparation and execution. Importantly, these processing stages were not sequential, instead overlapping both in time (**Fig. 2.3**) and cortical space (**Fig. 2.5**).

Thus, sustained stimulus-to-response HG activity temporally bridged stimulus processing with response execution across all tasks and participants. Next, we tested the hypothesis that sustained stimulus-to-response HG activation reflects

spatiotemporal information integration that translates stimulus characteristics into task-relevant behavioral output.

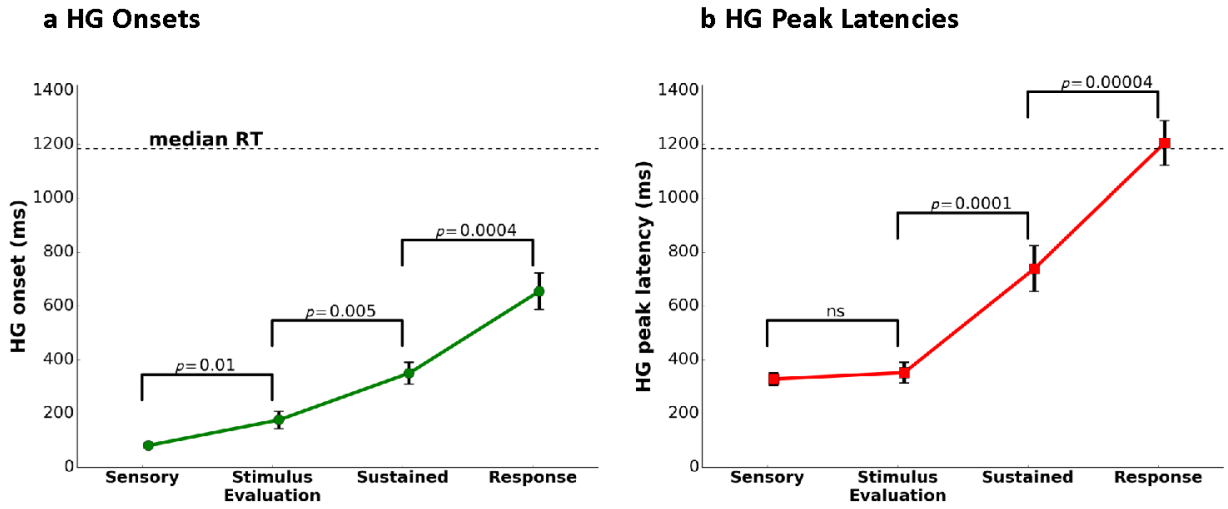

Figure 2.6 Sequential engagement of neuronal activation. Average HG onset times (**a**) and HG peak latencies (**b**) across datasets (from **Fig. 2.4**) are shown for each HG activation type: Sensory (N = 20), Stimulus Evaluation (N = 15), Sustained Stimulus-to-Response (N = 28), and Response (N = 29). Error bars denote s.e.m. across datasets. Median RT is calculated across all subjects and tasks for all response electrodes. Refer to **Fig. 2.4** for individual dataset data.

Behavioral relevance of sustained stimulus-to-response HG activity as evidence of spatiotemporal integration

To assess the behavioral relevance of the sustained stimulus-to-response activation, we first established that response times (RTs) across tasks were correlated with temporal features of the HG signal (using Pearson's correlation for all correlation analyses). Significant correlations were observed for both HG onsets ($r(26) = 0.82$, $p = 9.3\text{x}10^{-8}$; **Fig. 2.4a-b**) and HG peak latencies ($r(26) = 0.80$, $p = 3.9\text{x}10^{-7}$; **Fig. 2.4c**), with slower RTs associated with later engagement and peak of sustained stimulus-to-response activity. Similar correlations were observed for response activity (**Fig. 2.4a-c**), which is not surprising given that temporal proximity of HG onset and peak latency to response onset was the defining feature for this pattern of activation, but not for the sustained stimulus-to-response activity. In contrast, sensory and stimulus evaluation sites did not demonstrate a significant relationship between RTs and HG onset and only a moderate correlation for stimulus evaluation sites between RT and peak latency. This indicates that the link between timing of the sustained stimulus-to-response activity and RT cannot be attributed to differences in speed of sensory processing across participants, tasks, stimulus parameters or response modalities. Similar results were obtained when sources of variance were minimized by averaging across participants within each task (**Fig.**

2.7a) or by examining data from one participant who completed six tasks (**Fig. 2.7b**).

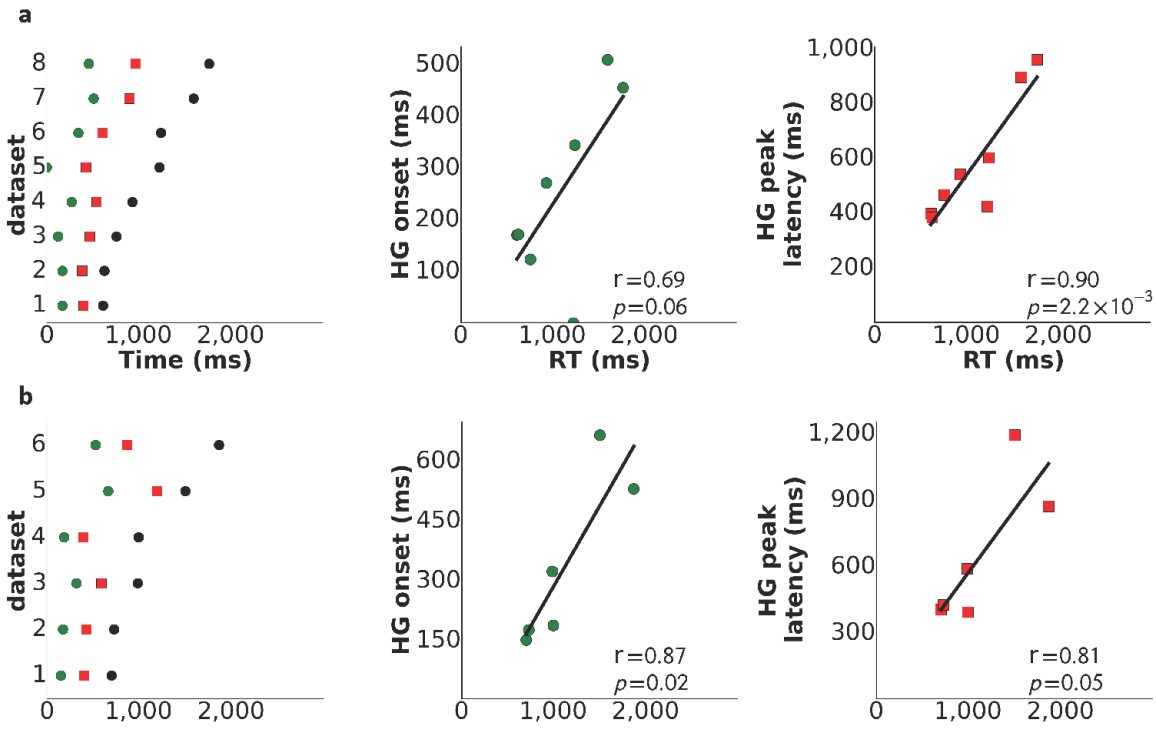

Figure 2.7: HG onset and peak latency of Sustained Stimulus-to-Response activity predict reaction times across tasks. (**a**) HG onsets and peak latencies for Sustained Stimulus-to-Response sites (left) along with correlations between reaction times and HG onsets (middle) or HG peak latencies (right) are presented for each task (N = 8), averaged across participants who completed that task. (**b**) Data in Panel a presented for one participant (S15) across tasks (N = 6). In both panels, data show similar patterns of strong correlations between reaction times and HG onset or peak latency seen in **Fig. 2.4**.

Having demonstrated the behavioral relevance of the temporal features of the sustained stimulus-to-response HG signal across tasks, we next examined whether sustained neural activity functionally linked stimulus and response processing across trials. First, all trials within each HG activation pattern for each task were pooled together and binned in 50 ms RT steps (**Fig. 2.8a**). This analysis revealed that temporal properties of the sustained HG signal and its relationship with other patterns of neural activation changed as a function of RT. As response times increased, sustained stimulus-to-response HG activity decreased in amplitude and extended in time relative to early bins (**Fig. 2.9**), indicating longer lasting but less pronounced neuronal firing. Specifically, sustained stimulus-to-response activity was characterized by a well-defined peak at short RTs, whereas longer RTs featured a plateau, with peak activity distributed across the trial window (**Fig. 2.8a**).

The magnitude of HG signal across the plateau time period was greater for sustained than for response activity ($t(58) = 12.84$, $p = 1.3\text{x}10^{-18}$), and the amplitude of sustained stimulus-to-response HG activity was negatively correlated with RTs ($r(28) = -0.89$, $p = 2.6\text{x}10^{-11}$; **Fig. 2.8b**). A stepwise regression between RTs and peak or mean values of the HG signal for each activity type revealed only two significant predictors (model $R^2 = 0.87$, $p = 7.0\text{x}10^{-13}$): the mean plateau amplitudes for the sustained stimulus-to-response activity (beta = -5.63, $p = 2.79\text{x}10^{-8}$) and the peak amplitude of response activity (beta = 2.02, $p = 4.75\text{x}10^{-4}$). In fact, while the magnitude of sustained stimulus-to-response activity decreased with longer RTs, the magnitude for the peak of response activity increased ($r(28) = 0.77$, $p = 5.4\text{x}10^{-7}$). In addition, the onset of sustained stimulus-to-response activity was delayed and overall diminished during trials on which participants failed to generate a response relative to successfully completed trials ($p<.05$, FDR-corrected; **Fig. 2.10a**), suggesting that sustained neuronal engagement during the stimulus-to-response window is essential for fast and successful response selection. Importantly, response activity was absent during no-response trials (all p-values>.05 FDR-corrected). Thus, we observed a clear functional dissociation between sustained stimulus-to-response and response activations. Since sustained stimulus-to-response activation is present during no-response trials where response activation is absent, we conclude that this sustained activity pattern indexes response selection but not motor preparation.

Next, we examined the relationship between temporal characteristics of the HG signal and RTs. As sustained stimulus-to-response activity began to decrease post-plateau, response activity increased, resulting in a critical crossover point, at which the two time series intersect. On average, the crossover point preceded RTs by 175.74 ms (s.e.m. = 9.34 ms), with a tight correlation between the crossover latency and RTs, $r(28) = 0.997$, 99%CI [0.992, 0.998], $p = 4.41\text{x}10^{-32}$ (**Fig. 2.8c**). The crossover latency was the only significant predictor in a stepwise regression ($R^2 = 0.99$, beta = 1.05, $p = 4.41\text{x}10^{-32}$) where it was entered along with HG onset, offset, and peak latency for sensory, stimulus evaluation, sustained stimulus-to response and response activity. Although other temporal parameters of HG signal correlated with RTs, none significantly contributed to the model, indicating that the crossover point is the time at which response selection implemented by the spatiotemporal integration network is complete and motor execution circuitry is initiated.

Sustained stimulus-to-response HG activity during stimulus integration

We next assessed whether and how sustained activity represents stimulus features relevant for response. First, if sustained stimulus-to-response activation integrates stimulus information, it must be temporally linked to stimulus processing. When tested, the offset of stimulus evaluation activity was the only significant predictor for the onset of sustained stimulus-to-response HG plateau (stepwise regression model $R^2 = 0.24$, beta = 0.8, $p = 5.50\text{x}10^{-3}$). The onset of the sustained plateau occurred 358.1 ms (s.e.m. = 27.55 ms) before the offset of stimulus evaluation

activity, suggesting that information transfer between the two systems is triggered prior to the completion of initial stimulus processing.

Further, we examined whether sustained stimulus-to-response activation is involved in stimulus representation in the Visual and Auditory Categorization tasks, where there is a one-to-one, direct correspondence between stimulus category and responses. In these tasks, 8.3% of sustained stimulus-to-response sites exhibited a category effect (significant HG modulation as a function of stimulus category: dog vs. cat or male vs. female, $p<.01$; **Fig. 2.10c**). We next examined the Antonym Generation task, where the response was dissociated from the stimulus category features. A stimulus category effect (noun vs. adjective) was observed in 10.4% of sustained stimulus-to-response sites. Thus, one of the functional roles of sustained stimulus-to-response activity is stimulus representation during response selection. Across these tasks, sites sensitive to the stimulus category effect were located on the PFC (middle and inferior frontal gyri; MFG, IFG), precentral gyrus, and sensory association cortex (**Fig. 2.10b**), reinforcing the role of the PFC and supporting areas in linking stimulus integration to response selection.

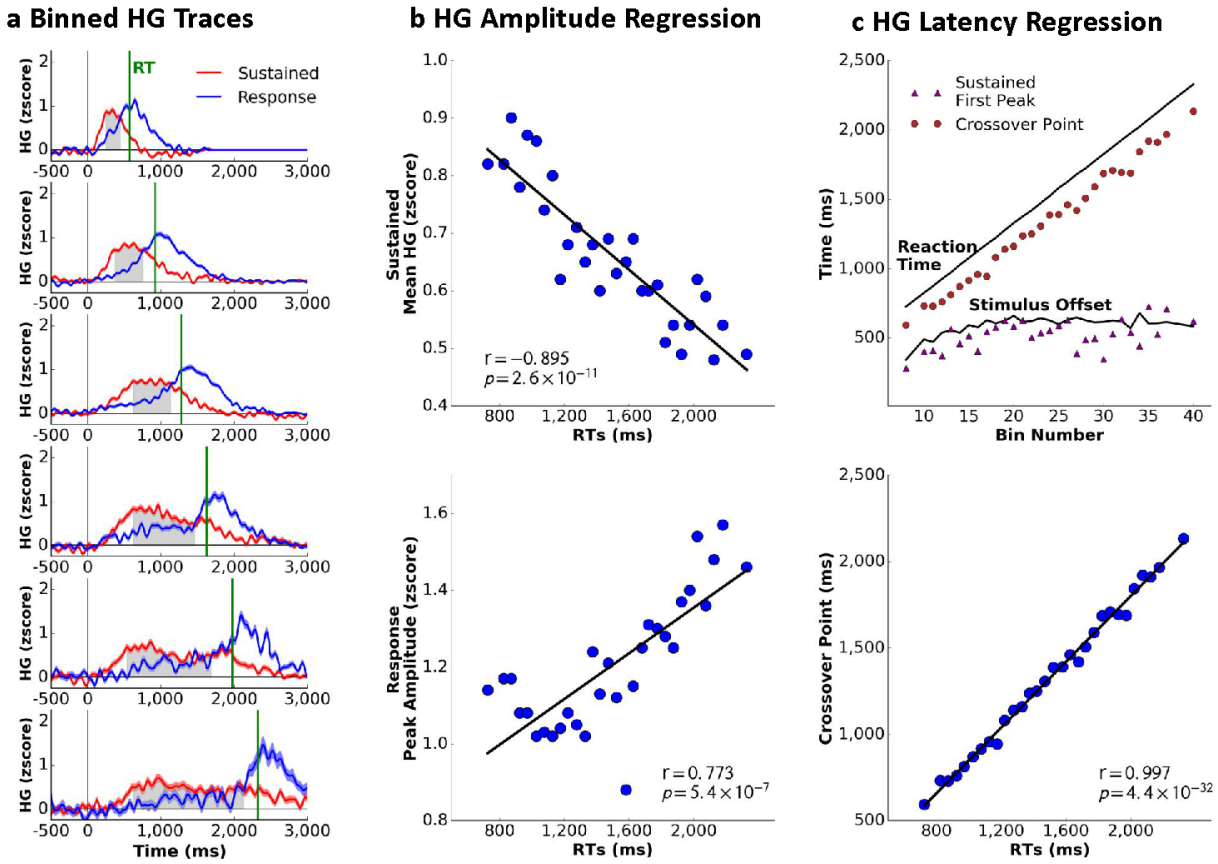

Figure 2.8 Interaction between sustained stimulus-to-response and response HG activity predicts reaction times. (**a**) The temporal evolution of the Sustained and Response HG activity varied as a function of reaction time. The Sustained Stimulus-to-Response plateau (from the first HG peak to the crossover point between Sustained and Response traces) is

shaded in gray. Shading on each trace indicates s.e.m. across trials for each time point (average number of trials per bin = 439 trials). (**b**) Longer reaction times were associated with smaller means for Sustained Stimulus-to-Response plateau (top) and larger peak amplitudes for Response activity (bottom). (**c**) The crossover point predicted reaction times, while the first peak of Sustained Stimulus-to-Response plateau tracked stimulus offset. N = 30 bins for (b) and (c).

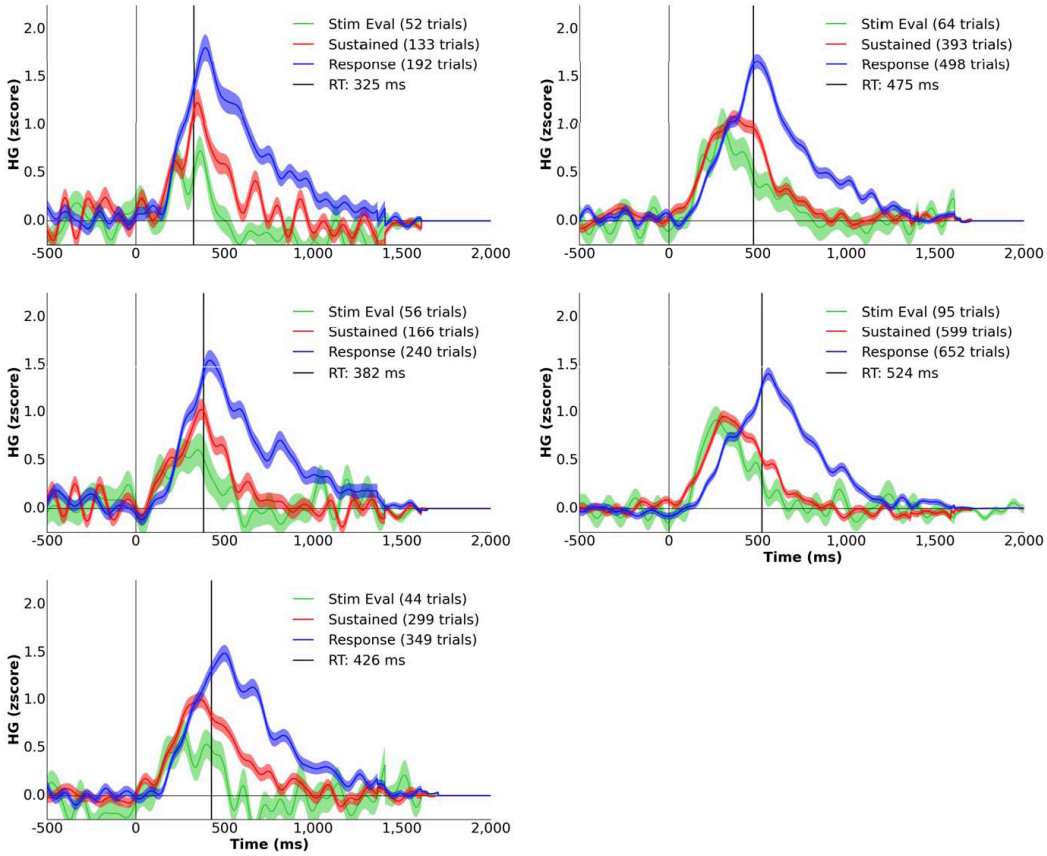

Figure 2.9 Fast response times rely on temporal convergence across HG activation types. Stimulus Evaluation, Sustained Stimulus-to-Response, and Response HG traces averaged across binned trials for fast reaction times (RTs between 300 and 550 ms). Shading for each trace indicates s.e.m. around the mean trace across trials. No traces for Sensory activation are shown as short RT trials came from participants whose electrode coverage did not feature this pattern. For short RTs, Sustained Stimulus-to-Response activity temporally overlapped with Stimulus Evaluation activity (mean difference between HG peak latencies 27.0 ms, s.e.m. = 17.09 ms; Mann-Whitney $U = 11$, $n_1 = n_2 = 5$, $p = 0.83$), with both closely tracking stimulus duration (HG peak latency for Sustained activity lagged behind stimulus offset by 51.46 ms, s.e.m. = 11.63 ms; $U = 0$, $n_1 = n_2 = 5$, $p = .01$). These findings suggest that fast cognitive processing and behavioral output may rely on temporal synchronization within local neuronal populations, as indexed by the temporal convergence of HG signals.

Task demands affect spatial and temporal profiles of integration

To investigate whether increased cognitive load modulates the spatial distribution and temporal characteristics of integration activity, we focused on data from the Word Repetition and Antonym Generation tasks recorded in three participants. Both tasks employed identical stimuli, yet required different levels of cognitive processing: Antonym Generation recruited semantic evaluation and search, absent during Word Repetition, resulting in longer RTs (S15: $t(259) = 15.08$, $p = 2.6\text{x}10^{-37}$; S18: $t(173) = 8.77$, $p = 1.6\text{x}10^{-15}$; S3: $t(144) = 14.74$, $p = 1.5\text{x}10^{-30}$) and greater RT variability (**Fig. 2.2**). We observed that although there was a considerable overlap in activation between the two tasks, more sustained stimulus-to-response sites were active during Antonym Generation than Word Repetition (**Fig. 2.11a**). The *overlap* sites were predominantly located on the IFG and precentral sulcus (reflecting a common substrate for word production(Flinker et al., 2015)), whereas sites *unique* to Antonym Generation were more broadly distributed throughout the left lateral PFC, indicating that task demands alter the spatial topography of integration activity (**Fig. 2.12**). In addition, while there were no significant differences between the two tasks in HG onsets of the *overlap* sites, sustained stimulus-to-response sites *unique* to Antonym Generation engaged later than *overlap* sites (**Fig. 2.11b**; Mann-Whitney test, S18: $U = 15.0$, $n_{overlap} = 10$, $n_{unique} = 7$, $p = .03$; S3: $U = 3.0$, $n_{overlap} = 11$, $n_{unique} = 6$; $p = 1.5*10^{-3}$; S15: $n_{overlap} = 6$, $n_{unique} = 11$,$U = 19.0$, $p = .09$). Notably, HG activation for *unique* Antonym Generation sites was comparable in amplitude across both short and long trials (no significant differences were detected), which excluded the possibility that engagement of *unique* sustained stimulus-to-response activation was due to task difficulty alone or was triggered by the temporal delay during response selection. Instead, these results indicate that engagement of additional cognitive operations (e.g., semantic search) necessary for successful Antonym Generation task performance is accomplished through sequential recruitment of additional computational resources, indexed by sustained stimulus-to-response integration activation.

Functional co-activation across different types of neuronal activity

Finally, we assessed functional interactions across different activation patterns within each dataset using PCA conducted on mean HG amplitudes across trials. The first principal component, which accounted for 24.81% variance (s.e.m. = 1.85%) across all tasks, revealed a distributed network of sites, with HG activity co-modulating on a trial-by-trial basis. Most cortical sites with sustained stimulus-to-response activity (57%) were a part of this primary functional network, which also included all other types of HG activity patterns (**Fig. 2.13a**), indicating that although sustained integration activity accounts for the majority of task-relevant cortical activation, it is functionally connected with both stimulus processing and response execution sites.

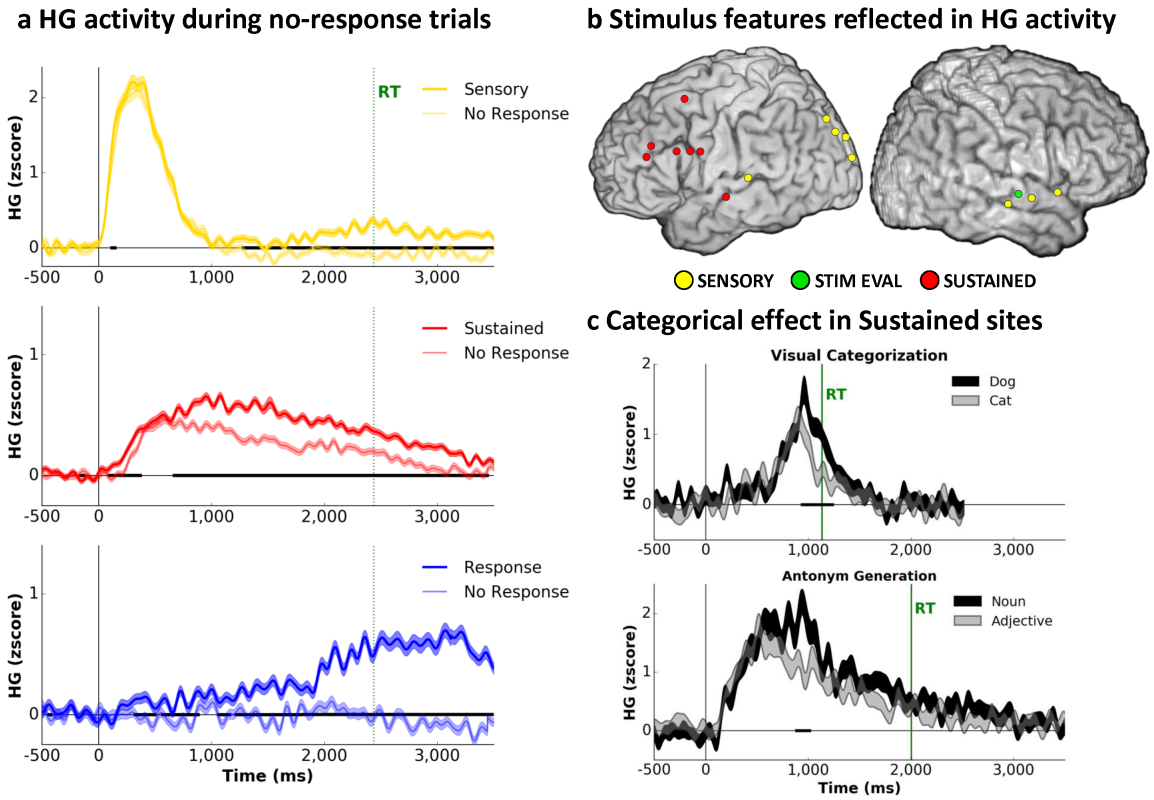

Figure 2.10 Spatiotemporal Integration is critical for stimulus representation and response selection. (**a**) Average traces for the Sensory (N = 570), Sustained Stimulus-to-Response (N = 1734), and Response (N = 596) HG patterns for trials with and without a response (matched numbers of trials) in the Antonym Generation task. (**b**) Sustained Stimulus-to-Response sites exhibiting a category effect in the Antonym Generation and Visual and Auditory Categorization tasks (N = 7 subjects). (**c**) Representative Sustained Stimulus-to-Response sites showing a category effect in the Visual Categorization task (dog, N = 91 vs. cat, N = 90) and a part of speech effect in the Antonym Generation task (noun, N = 78 vs. adjective, N = 69). Shading on each trace indicates s.e.m. across trials for each time point. Black bold segments along the x-axis indicate significant differences between traces.

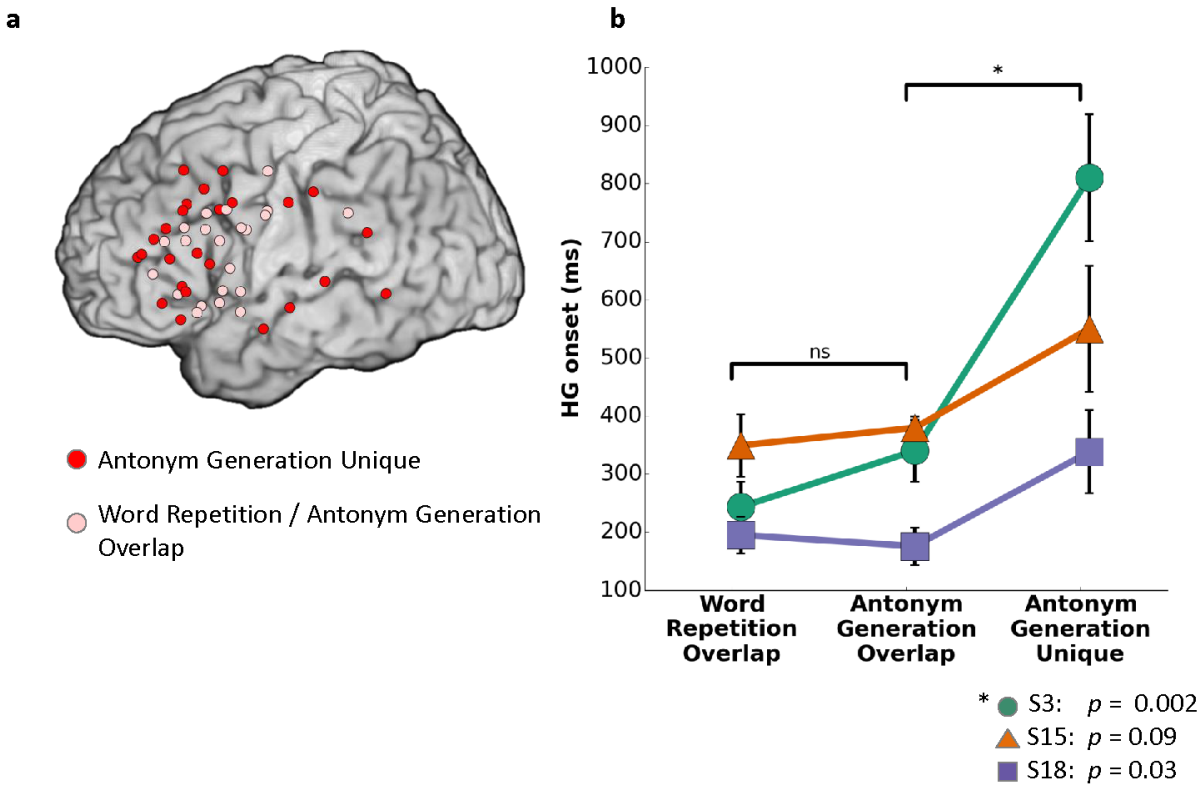

Figure 2.11 Task demands affect spatial and temporal profiles of integration.
(**a**) Sustained Stimulus-to-Response sites active during both Word Repetition and Antonym Generation tasks (*overlap*, N = 24) were predominantly restricted to the inferior frontal gyrus. In contrast, Sustained Stimulus-to-Response sites active only during Antonym Generation task (*unique*, N = 24) were more broadly distributed across cortex. (**b**) Sustained Stimulus-to-Response HG activity onsets averaged across *overlap* sites in Word Repetition, *overlap* sites in Antonym Generation, and *unique* sites in Antonym Generation (S3: $N_{overlap} = 11$, $N_{unique} = 6$; S15: $N_{overlap} = 6$, $N_{unique} = 11$; S18: $N_{overlap} = 10$, $N_{unique} = 7$). Error bars denote s.e.m. across sites.

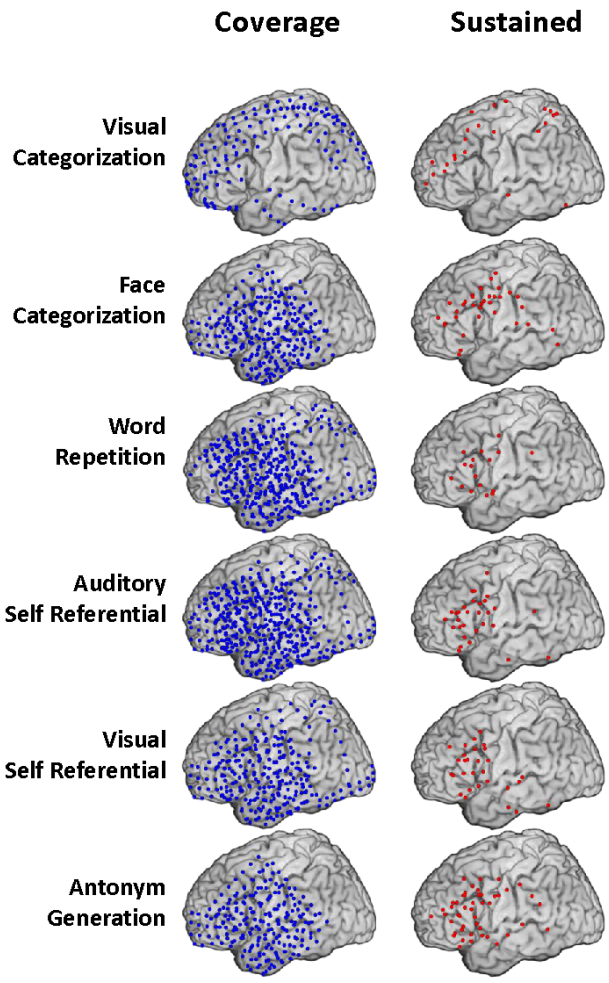

Figure 2.12 Task-specific cortical distribution of Sustained Stimulus-to-Response sites. Electrode coverage and cortical distribution of Sustained Stimulus-to-Response sites for tasks with left hemisphere electrode coverage, sorted in ascending order of RT (top to bottom). Gender and Emotion Face Categorization tasks are combined into a single image because there was 95% overlap in cortical coverage. Linguistic tasks featured greater proportion of Sustained Stimulus-to-Response sites over the inferior frontal gyrus (IFG; 74.7%) relative to the middle frontal gyrus (MFG; 33.3%), whereas non-linguistic tasks (Visual Categorization and Face Categorization) had greater distribution of sustained stimulus-to-response sites on the MFG (48.7%) relative to IFG (16.7%).

a Functional Network Analysis

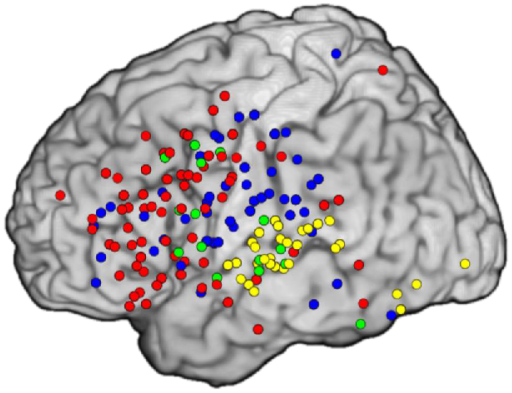

Electrode Types	Primary Network	
	% of each type in PC1	% of all PC1 electrodes
SENSORY	49%	22%
STIM EVAL	54%	14%
SUSTAINED	**57%**	**37%**
RESPONSE	45%	27%

b Domain-General fMRI Activation (meta-analytic inference)

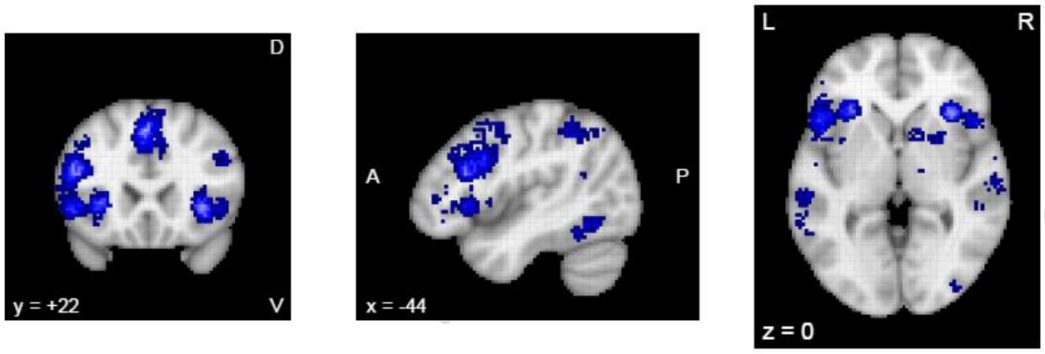

Figure 2.13 Functional connectivity analyses. (**a**) Principal component analyses performed within each dataset (using mean HG amplitude values calculated in the activation window for each trial) revealed a network of distributed sites linked by correlated trial-by-trial HG activity. Most Sustained Stimulus-to-Response sites (57%) belonged to the first principal component (PC1); however, this network also included 63% of sites with other types of HG activity. (**b**) Algorithm-generated (neurosynth.org) meta-analysis of significant fMRI activations (N = 2399) among published papers (N = 61) using the term "domain-general" (forward inference – probability of an activation being present given that a paper uses the specified term; p = .01, FDR corrected). These areas of activation closely correspond to brain regions exhibiting Sustained Stimulus-to-Response activation in the current study.

2.4 Discussion

Capitalizing on the superb temporal resolution and spatial specificity of direct cortical recordings, we demonstrate that intrinsically sustained stimulus-to-response activation, centered in the PFC, provides the foundation for linking perception and action in humans on a single trial basis. This sustained neuronal activity is functionally coordinated in time and across cortical space, providing spatiotemporal integration of information that binds stimulus processing with response execution with remarkable precision.

Temporally, information integration was reflected in intrinsically sustained neuronal activation, triggered during initial stimulus processing and lasting until the response. Stimulus, sustained, and response processing occurred in sequential progression with partially overlapping stages, confirming previous research on region-specific processing timescales in nonhuman primates (Murray et al., 2014 ; Siegel et al., 2015). Spatially, sustained activation was centered in the PFC, which is known to have strong anatomical connections with other cortical regions that also showed stimulus-to-response activation (Catani et al., 2012 ; Sreenivasan, Curtis, & D'Esposito, 2014). Notably, areas with sustained stimulus-to-response HG activity closely mapped onto brain regions exhibiting significant fMRI activation in studies describing domain-general processing (Duncan & Owen, 2000 ; Fedorenko et al., 2013 ; Yarkoni, Poldrack, Nichols, Van Essen, & Wager, 2011) (**Fig. 2.13b**). Thus, this cortical network provides an ideal anatomical and physiological substrate for information exchange and integration among distributed local cortical networks (Miller & Cohen, 2001). Functionally, sustained stimulus-to-response activity bridged stimulus processing with response execution. Specifically, modulation in amplitude of this activity reflected stimulus features, scaled with cognitive demand and successful task performance, and was linked to response speed. Additionally, trial-by-trial amplitude modulation of the sustained stimulus-to-response network was correlated with activity within both stimulus and response sub-networks.

Animal and human studies indicate that HG activity is correlated with increased fMRI BOLD signal (Mukamel et al., 2005 ; Mukamel & Fried, 2012), reflecting increased firing among local neuronal populations (Ray et al., 2008 ; Ray & Maunsell, 2011). Our findings indicate that increasingly coordinated neuronal firing across multiple neuronal ensembles is required for fast behavioral responses, evident from both the temporal convergence and the high amplitudes of sensory, sustained, and response HG activity for short RT trials. In contrast, decreased response certainty and longer RTs are associated with less temporally coordinated and attenuated local neuronal activity.

Critically, sustained neuronal activity does not reflect a single localized process. Instead, we observed activity distributed in time, space, and function. Spatially, cortical distribution of sustained activation varied with task demands. For example,

in line with previous research, linguistic tasks primarily recruited sustained activation in the IFG/Broca area (Fedorenko et al., 2012 ; Flinker et al., 2015 ; Sahin, Pinker, Cash, Schomer, & Halgren, 2009), whereas non-linguistic tasks relied on other PFC regions (e.g., MFG, superior frontal gyrus, and premotor regions). Further, as task difficulty and cognitive processing demands increased, we observed broader cortical recruitment during the spatiotemporal integration epoch. Temporally, we found that different processing stages were triggered at different times, based on task demands. Finally, not all integration sites performed similar functions, as only a subset of sustained activation sites was active in different tasks. Thus, sustained activity reflects the cumulative output of local neuronal networks, in which some neurons exhibit sustained firing while others may exhibit specific tuning to particular stimulus dimensions or response contingencies.

In conclusion, this study demonstrates that intrinsically sustained neuronal activity in the stimulus-to-response window provides a common functional substrate for information integration and response selection across diverse cognitive tasks. We identify the prefrontal cortex as the core element of a distributed cortical network that links stimulus perception with action execution, enabling humans to flexibly respond to ever-changing environmental demands.

Table 2.1 Participant information

Subj.	Gender	Age	Hand.	Lang. Lat.	Num. elecs.	Num. active	Electrode Coverage
S1	male	30	right	NA	90	31	ATL, Area 37, IFG, FrP, InfTL, MFG, mPC, OFC, PostCG, PreSMA, PreCG, R_IFG, R_IPL, R_InfT, R_MFG, R_MTG, R_mPC, R_PostCG, R_PreSMA, R_PreCG, R_SFG, R_SMA, R_SPL, R_STG, R_dACC, SMA, STG, dACC
S2	female	36	right	left	99	58	ATL, Area 37, IFG, IPL, ITG, InfTL, MFG, MTG, OFC, Occip, PostCG, PreCG, R_ATL, R_InfT, STG
S3	male	38	left	left	103	38	ATL, Area 37, IFG, FrP, IPL, ITG, InfTL, MTG, OFC, PostCG, PreCG, STG
S4	male	16	right	NA	62	22	ATL, Area 37, IFG, IPL, MTG, PostCG, PreCG, STG
S5	male	19	right	left	89	28	ATL, Area 37, IFG, IPL, ITG, MFG, MTG, PostCG, PreCG, STG
S6	male	20	right	left	70	10	R_ATL, R_IFG, R_MFG, R_MTG, R_PreSMA, R_PreCG, R_SFG, R_STG, R_dACC, dACC, preSMA,
S7	male	42	right	NA	104	37	IFG, FrP, IFG, IPL, MFG, OFC, Occip, PostCG, PreSMA, PreCG, SFG, SPL, STG, dACC
S8	female	22	right	left	81	31	Area 37, FrP, IPL, MFG, mPFC, mPC, Occip, PCC, PostCG, PreSMA, PreCG, SFG, SMA, SPL, STG, dACC
S9*	male	47			EXCLUDED		
S10	female	32	right	left	80	24	IFG, FrP, ITG, MFG, MTG, OFC, PostCG, PreCG, SMA, SPL, STG, mPFC, preSMA
S11	female	19	right	NA	90	18	FrP, mPC, PCC, PreSMA, R_Area 37, R_FrP, R_IPL, R_ITG, R_MTG, R_mPC, R_PCC, R_PreSMA, R_SMA, R_SPL, R_STG, R_dACC, SMA, dACC,
S12	male	42	left	NA	74	15	IPL, ITG, MFG, MTG, mOccip, mPC, Occip, PCC, PostCG, PreCG, R_mOccip, R_mPC, R_PCC, SPL, STG
S13	male	19	right	NA	108	18	R_OFC, R_FrP, R_IFG, R_PreCG, R_PostCG, R_STG, R_MTG, R_ATL,

							R_Area 37, R_IPL, R_Occip, R_MFG, R_InfTL, R_SPL
S14	male	47	NA	NA	97	40	R_FrP, R_IFG, R_MFG, R_PreCG, R_PostCG, R_STG, R_MTG, R_ATL, R_Area 37, R_IPL, R_Occip, R_IftTL
S15	male	34	right	left	74	45	ATL, Area 37, IFG, IPL, MFG, MTG, PostCG, PreCG, STG
S16*	male	37	right		EXCLUDED		
S17	male	22	right	left	60	29	R_ATL, R_IFG, R_IPL, R_MFG, R_MTG, R_PostCG, R_PreCG, R_STG
S18	male	48	left	left	63	47	ATL, Area 37, IFG, IPL, MFG, MTG, PostCG, PreCG, STG

Note: Unless otherwise specified (R_), all cortical areas are in the left hemisphere.
(*) Participants S9 and S16 were excluded due to stroke-related cortical lesion (S9) and unconfirmed electrode localization (S16).
Abbreviations: Hand. – Handedness, Lang. Lat. – Language Laterality, NA – information not available, Num. elecs. – Number of recorded electrodes, Num. active – Number of task active electrodes, Part. – Participant;
Area 37 – Brodmann area 37, ATL – anterior temporal lobe, dACC – dorsal anterior cingulate cortex , IFG – inferior frontal gyrus, FrP – frontal pole, IPL – inferior parietal lobule, InfTL – inferior temporal lobe, ITG – inferior temporal gyrus, MFG – middle frontal gyrus, mPC – medial parietal cortex, mPFC – medial prefrontal cortex, MTG – middle temporal gyrus, OFC – orbital frontal cortex, Occip – Occipital lobe, mOccip – medial occipital lobe, PCC – posterior cingulate cortex, PostCG – post central gyrus, PreSMA – pre-supplementary motor area, PreCG – pre-central gyrus, SFG – superior frontal gyrus, SMA – supplementary motor area, SPL – superior parietal lobule, STG – superior temporal gyrus

Table 2.2 Task information

Task / Participant	Number of Stimuli per Block	Number of Blocks Completed	Number of Analyzed Stimuli	RT (ms)	
				mean	s.e.m
Visual Categorization	**75**			**765.51**	**130.77**
S8	(1 unique	6	413	896.28	9.51
S10	block)	4	273	634.74	7.08
Auditory Categorization	**75**			**1,554.73**	**90.63**
S13	(1 unique	4	124	1,464.10	53.88
S14	block)	4	260	1,645.36	8.86
Word Repetition	**105**			**1,117.70**	**118.72**
S1	(2 unique	2	138	1,310.55	19.83
S2	blocks)	1	50	1,170.04	15.73
S3*		2	83	934.53	9.08
S4		2	136	1,086.18	15.86
S7		1	74	1,376.84	31.93
S11		2	135	946.54	11.59
S12		2	144	1,145.16	11.44
S15		2	114	1,003.20	12.09
S18		2	85	903.06	16.89
Antonym Generation	**105**			**2,050.27**	**426.18**
S3	(2 unique	2	63	1,983.10	80.90
S6	blocks)	4	133	2,841.18	90.40
S15		3	147	2,002.87	57.46
S18		2	90	1,373.91	45.54
Face Emotion Categorization	**80**			**643.52**	**68.40**
S3	(2 unique	2	113	690.90	12.63
S5	blocks)	2	112	532.12	11.58
S15		2	131	750.92	13.55
S18		2	104	600.12	16.57
Face Gender Categorization	**80**			**626.95**	**90.91**
S15	(2 unique	2	131	717.86	12.28
S18	blocks)	2	83	536.04	17.79
Auditory Self Referential	**132**			**1,719.82**	**163.73**
S1	(1 unique	1	61	1,811.82	49.94
S2	blocks)	1	61	1,592.69	55.71
S3		1	57	1,597.42	44.12
S5		1	72	2,113.94	88.37
S6		1	89	2,028.34	69.25
S7		1	88	1,752.06	45.50
S11		1	78	1,665.19	68.31

S12		1	43	1,688.14	123.23
S15		1	82	1,657.04	57.51
S17		1	74	1,291.51	49.94
Visual Self Referential	**132**			**1,460.24**	**188.29**
S2	(1 unique	1	64	1,297.61	41.52
S3	blocks)	1	50	1,642.44	66.23
S12		1	65	1,627.05	56.82
S15		1	77	1,068.06	36.01
S17		1	84	1,666.06	62.49

* Subject S3 was used for Task Demands analysis only (**Figure 2.11**). It was excluded for all other analyses due to insufficient RT range to discriminate among different types of HG activation (see Methods – Cluster Classification).

Chapter 3

Algorithmic identification of oscillatory frequency and bandwidth

Abstract

Neuronal communication is intricately tied to oscillatory dynamics within and across cortical regions. Despite the acknowledged variability in oscillatory frequency, the majority of research uses predefined canonical frequency bands. Here we introduce a novel method for algorithmically extracting individualized oscillatory bands. We first validate the algorithm against synthetically generated data and show that it is as sensitive as expert human labelers. We then apply this method to data recorded at different electrophysiological scales: local field potentials in non-human primates and human scalp EEG. We find striking heterogeneity in center frequency and bandwidth in both populations, with the two oscillatory parameters predicting subject identification with high degree of accuracy. Using individualized filters, we unmask correlations between behavior and EEG alpha power that are missed by canonical band filtering. Finally, we demonstrate that faster oscillations have broader bandwidths in both populations, and that these two individualized parameters predict visual working memory precision in non-human primates. This method provides a new tool for studying individual differences in oscillatory physiology and function.

3.1 Introduction

Cognitive processes are supported by computation in distributed neuronal networks. Communication between these networks may rely on oscillatory dynamics both within local neuronal populations and across disparate brain regions. Research suggests that oscillatory power and phase of low frequency (< 40 Hz) bands influences a variety of cognitive, perceptual, and behavioral tasks (Busch, Dubois, & Vanrullen, 2009 ; Samaha & Postle, 2015 ; Schroeder & Lakatos, 2009). Furthermore, dysfunctions in oscillatory activity have been implicated in nearly every major neurological and psychiatric disorder (Voytek & Knight, 2015), including Parkinson's (de Hemptinne et al., 2015), schizophrenia (Uhlhaas & Singer, 2010), depression (Segrave et al., 2010), and autism (Khan, Gramfort, & Shetty, 2013). Given the clear physiological importance of neural oscillations, much research has been dedicated to examining the nature and function of oscillatory activity in the brain and its behavioral relevance.

The vast majority of these studies utilize classic, canonical bands of interest, approximately defined as: delta, 1-4 Hz; theta, 4-8 Hz; alpha, 8-12 Hz; beta, 15-30 Hz, and; gamma, > 30 Hz. However these frequency bands are only loosely related to the underlying physiology, and there exists a great deal of variability across species (Bullock, 1981), age (Klimesch, 1999 ; Obrist, 1954), and cognitive/behavioral state (Haegens, Cousijn, Wallis, Harrison, & Nobre, 2014 ; Samaha & Postle, 2015 ; Samaha, Bauer, Cimaroli, & Postle, 2015). Predetermined frequency bands may include noise from outside the true physiological oscillatory band – center frequency and bandwidth of which may not coincide with a canonical pass band – thus masking crucial behaviorally and physiologically relevant information. Current methods for identifying individual differences in oscillations are mostly restricted to identifying the frequency at which the power spectrum peaks within a specific sub-band, however these methods are susceptible to noise and are limited to finding only one oscillation while ignoring other potentially physiologically relevant oscillations as well as oscillatory features, such as bandwidth.

To address this issue we have developed a novel statistical model for algorithmically extracting individualized oscillatory components. This algorithm extracts oscillation center frequencies and their associated bandwidths, as well as the background 1/*f* noise parameter (**Fig. 3.1**). This Fitting Oscillations and One-over F algorithm is validated against simulated power spectra that are generated to include varying levels of noise and combinations of oscillatory parameters (center frequency, bandwidth, power, and number of oscillations). These synthetic data, which have known underlying oscillatory components, provide a dataset against which we compare algorithmic performance to that of expert human labelers. We then use the algorithm to extract oscillatory components from non-human primate local field

potentials (LFP) and human scalp electroencephalography (EEG) recorded while subjects performed a working memory task.

We find that by using individualized filters appropriate for the signal of interest in humans, correlations between working memory load and alpha amplitude that are missed by canonical filtering are unmasked. We also find that individual differences in both center frequency and bandwidth relate to working memory precision in non-human primates. Additionally, these oscillatory parameters are interrelated, hinting at their underlying physiological origins and functions. In contrast to predefined canonical band analyses, we provide a new algorithm for investigating both the physiological origins of oscillations and the role that oscillatory variability may play in explaining individual differences in cognitive functioning in health, aging, and disease.

3.2 Methods

Subjects

Humans

We collected 64-channel scalp EEG from young (20-30 years old), healthy controls (n = 11; 5 male). All participants gave informed consent approved by the UC Berkeley Committee on Human Research.

Non-human primates

Two male rhesus monkeys (Maccaca mulatta; 4-5 years old) participated in the study. All procedures were in accord with the US National Institutes of Health guidelines and the recommendations of the UC Berkeley Animal Care and Use Committee. These data were previously published, and methodological details can be found in the corresponding manuscript (Lara & Wallis, 2014).

Tasks and stimuli

Humans

The visual working memory paradigm was slightly modified from the procedures used in (Vogel & Machizawa, 2004) as outlined in (Voytek & Knight, 2010) where additional task details can be found. Participants were visually presented with a fixation cross in the center of the screen throughout the entire duration of the experiment. At the beginning of each trial, this cross would flash to signal the beginning of the trial. This was followed 350 ms later by one, two, or three different colored squares for 180 ms, lateralized to either the left or right visual hemifield. After a 900 ms delay, a test array of the same number of colored squares appeared in the same spatial location. Participants were instructed to respond with a button press to indicate whether or not one item in the test array had changed color compared to the initial memory array. Each participant performed 8 blocks of 40 trials each. Data were analyzed from visual cortical alpha electrodes contralateral

to the hemifield of visual stimulus presentation (channels P3/5/7/9, PO3/7, and O1 for right hemifield stimuli and P4/6/8/10, PO4/8, and O2 for left hemifield stimuli).

Non-human primates
Subjects were trained on a color detection task as previously described in (Lara & Wallis, 2014). Briefly, a fixation square appeared at the start of each trial followed by a sample array of one or two colored squares (500 ms). During the subsequent 1000 ms delay, the subjects had to maintain the square colors in working memory. After the delay, one of the squares was presented again and the subject had to indicate via a lever press whether the color at the location changed or remained the same.

Data acquisition and preprocessing
Humans
Participants were tested in a sound-attenuated EEG recording room using a 64+8 channel BioSemi ActiveTwo system. EEG data were amplified (-3dB at ~819 Hz low-pass, DC coupled), digitized (1024 Hz), and stored for offline analysis. Horizontal eye movements (HEOG) were recorded at both external canthi; vertical eye movements (VEOG) were monitored with a left inferior eye electrode and superior eye or fronto-polar electrode. Participants were instructed to maintain central fixation and responded using the index finger of their right hand. All data were referenced offline to the average potential of two earlobe electrodes. Scalp EEG artifacts (electrode drifts, blinks, and saccades) were identified on a semi-automated basis. All incorrect trials and trials with artifacts were excluded from analysis. Raw time series data were filtered as outlined below to passband extract analytic amplitude. These analytic amplitude time series were then subjected to standard event-related analyses.

Behavioral accuracy was assessed using a d' measure of sensitivity which takes into account the false alarm rate to correct for response bias. To avoid mathematical constraints in the calculation of d', we applied a standard correction procedure wherein, for any subjects with a 100% hit rate or 0% false alarm rate, performance was adjusted such that 1/(2N) false alarms were added or 1/(2N) hits subtracted where necessary.

Non-human primates
Neuronal responses were recorded simultaneously from PFC using arrays of 8-32 tungsten microelectrodes. Local field potentials were recorded with a 1 kHz sampling frequency and analyzed offline. LFP were isolated from the band-passed (0-100 Hz) recordings, and spectral fits were done on a channel-by-channel basis. See (Lara & Wallis, 2014) for recording details.

Similar to the prior study, a median split was used to separate low- and high-oscillatory power trials. For each band and high/low power trial grouping, the

working memory precision (σ_{WM}) with which the two-color memory arrays were stored was estimated using the behavioral model described previously. We could then estimate how the band-specific oscillatory parameters of center frequency and bandwidth relate to working memory precision estimates.

Algorithmic fitting of 1/f function and oscillatory components

We characterize neural power spectra using two components: a background power law (1/*f*) process and a set of independent and additively overlaid oscillations, characterized as peaks or bumps atop the 1/*f* background (Buzsaki, Logothetis, & Singer, 2013 ; He, 2014 ; Wang, 2010). The goal of the algorithm is to identify the center frequency and bandwidth of the oscillatory components, so it is critical to isolate them from the 1/*f* background. To achieve this, we need to accurately represent the background 1/*f* process. Because power laws are linear in log space, we estimate the exponent χ of the spectral power law by $log(S(f)) = \chi(log(f))$ where f is frequency and S is the spectral power. Oscillatory peaks superimposed on top of the 1/*f* background act as outliers, drawing the estimate χ_{est} away from its true value χ. To compensate for this, we use a robust linear model (Random Sample Consensus (Fischler & Bolles, 1981)) that minimizes the influence of these oscillatory components on χ_{est}.

The power law 1/*f* trend, χ_{est} is then subtracted from the original PSD (**Fig. 3.1a**). This flattens the power spectrum, isolating the oscillatory components, giving $S_{flat}(f) = S(f) - f\chi_{est}$. This flattened power spectrum is dominated by oscillatory components, with small non-linear deviations (*i.e.*, noise). These deviations are removed by thresholding S_{flat}, reducing these noise deviations to zero while keeping the oscillatory components intact (**Fig. 3.1b**). Any deviations below the 1/*f* background are also set to zero. The threshold for S_{flat} was set to a value of 0.01.

The next step is to identify and model the oscillatory components in the flattened power spectrum. Previous work has shown that single Gaussians provide good estimates of single alpha peaks(Haegens et al., 2014). Given that a neural power spectrum typically contains multiple oscillatory components, we use a Gaussian Mixture Model (GMM) to decompose the flattened spectrum into an optimal number of Gaussians, estimating the center frequency (f_c, mean), bandwidth (ς, standard deviation), and relative probability density of each. Since GMMs operate on data from normally distributed random variables, we converted continuous analytic power spectra values into discrete distributions binned by frequency This is accomplished by representing log power estimates as value counts for each frequency, f_i, where the number of count entries for each frequency is linearly proportional to its log power $log(S(f))$ (**Fig. 3.1c,d**).

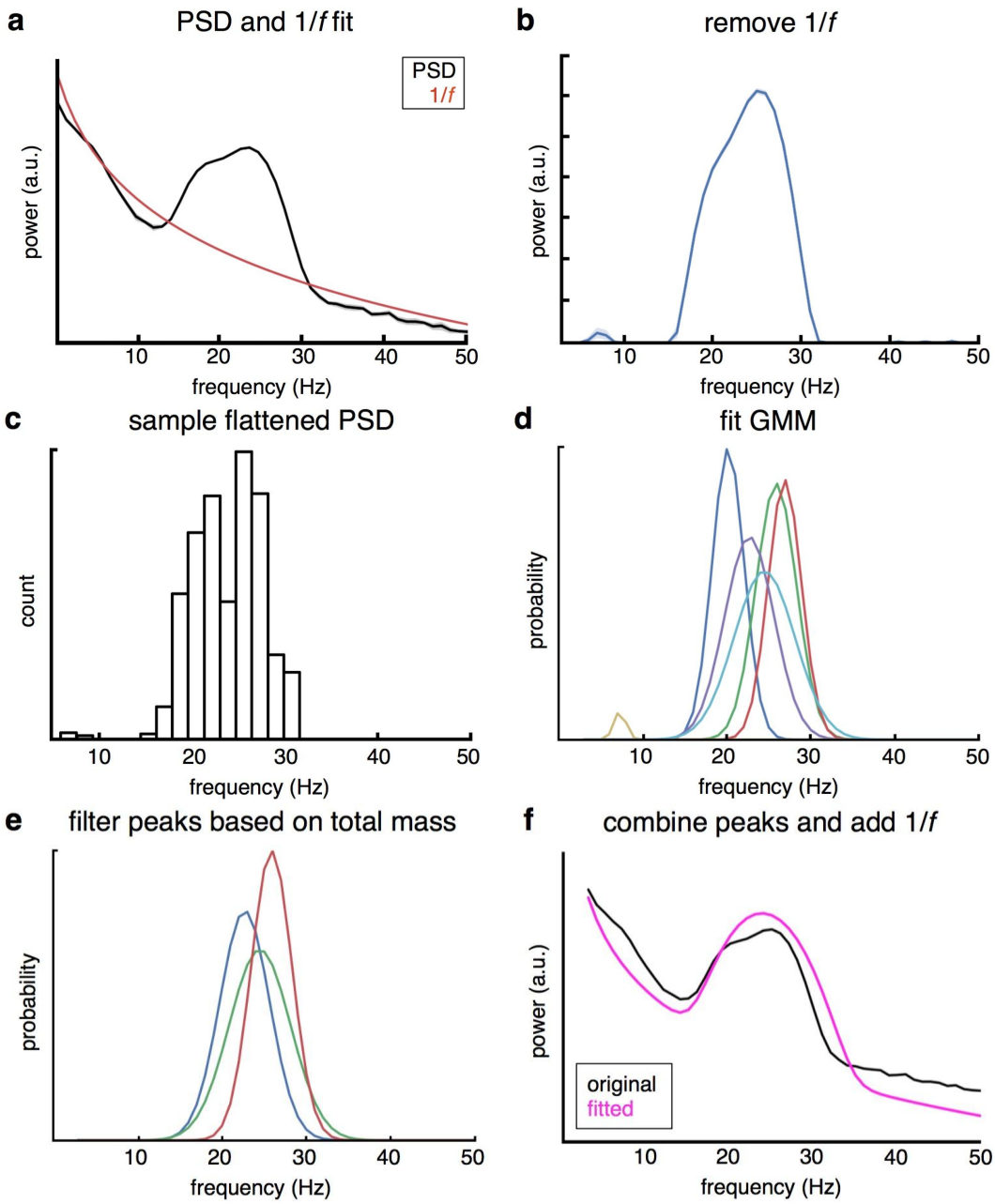

Figure 3.1 Algorithm schematic. (**a**) Calculate power spectral density (PSD). Fit 1/f background power using robust linear fit. (**b**) Subtract background power from original PSD, yielding flattened PSD. (**c**) Sample from flattened PSD as if it were a probability density function. (**d**) Fit Gaussian Mixture Model selecting number of components using BIC model comparison approach, and calculate probability density function for each peak. (**e**) Filter peaks to exclude those with total mass less than min_p parameter. (**f**) Combine peaks that are closer together than predetermined frequency threshold and add 1/f fit back into model.

The number of peaks in the GMM was minimized via model comparisons, using the conservative Bayesian information criterion (BIC) to weight alternate models (Schwarz, 1978). From a maximum of 10 possible peaks, the model with the

smallest BIC score that was at least eight BIC units smaller than the next option was selected. The number of maximum allowed peaks (ten) was chosen as a reasonable prior well above the plausible upper bound for the number of expected *a priori* independent oscillations in the signal, assuming the 5 traditional delta, theta, alpha, beta, and gamma bands also split into "upper" and "lower" sub-bands. A minimum difference of eight BIC units represents strong evidence that the smaller-valued model is a better and maximally parsimonious fit (Burnham, 2004). GMM peak fitting was done with expectation maximization, based on a log-likelihood loss function (Pedregosa, Varoquaux, & Gramfort, 2011).

To control for false positives, GMM-defined peaks were subjected to additional refinement. Peak refinement was based on the total probability mass present in each candidate GMM peak, *i.e.*, the marginal relative probability of that peak compared to all peaks combined. Peaks below the minimum probability (min_p) were excluded (**Fig. 3.1e**). The minimum probability threshold was determined separately for each dataset. This post-fit exclusion effectively minimized false positives introduced by frequency-independent noise and due to incomplete removal of nonlinear cross-frequency warping sometimes present in the flattened spectra (the two most common failures modes of the algorithm based on pilot tests on synthetic, human scalp EEG, and non-human LFP data). Finally, any two peaks with centers within $2r$, where r is the spectral resolution (1 Hz), were combined, correcting for occasional overfitting by the GMM expectation maximization algorithm. Overall, *post hoc* peak refinement proved more effective in balancing recall and precision than additional preprocessing, *i.e.*, greater smoothing of the spectra prior to application of the algorithm.

There is a tradeoff between recall and precision as a function of probability threshold, so the threshold that equalized precision and recall was selected (**Fig. 3.2**). Recall and precision are used in an information retrieval sense, where recall is the proportion of peaks identified compared to total peaks, and precision is the proportion of correctly identified peaks compared to the number of detected peaks plus number of false positives; in other words, precision is the proportion of retrieved items that are relevant such that high precision reflects few false positives, whereas recall (also known as sensitivity) is the proportion of relevant items that are retrieved such that high recall reflects few false negatives.

In the final step, the fitted peaks are recombined with the original $1/f$ fit to give an estimated reconstruction of the original PSD that can be then used for visual inspection and manual verification of algorithm performance (**Fig. 3.1f**). The final output of the algorithm consists of center frequency and bandwidth estimates for each fitted oscillatory peak, in addition to the reconstructed PSD estimation. All preprocessing and fitting was done in the Python programming language, with fitting of both χ and oscillatory peaks done using the scikit-learn machine learning

library (Pedregosa, Varoquaux, & Gramfort, 2011). Full source code and detailed usage examples are available at https://github.com/voytekresearch.

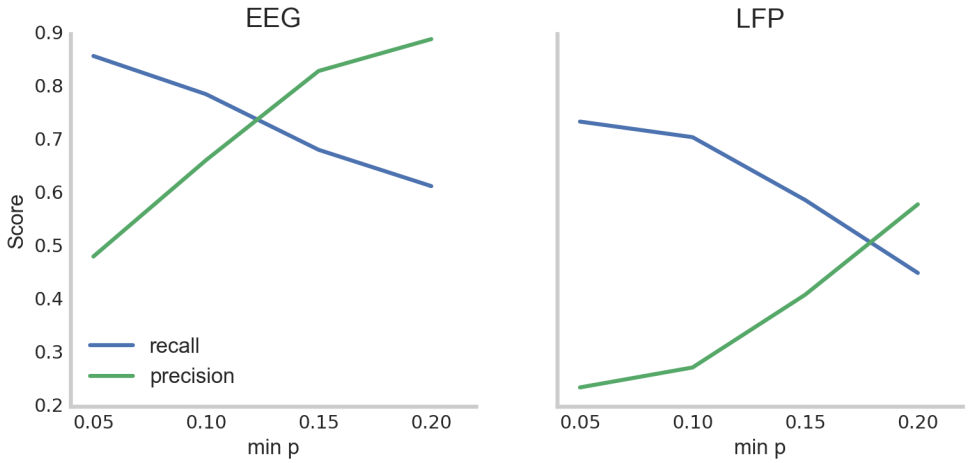

Figure 3.2 Tradeoff between precision and recall for algorithm performance on EEG and LFP datasets. Precision and recall values are affected by the minimum probability threshold for GMM-defined peaks. As the minimum probability threshold increases, recall values decrease, reflecting decreased sensitivity and more false negatives. Precision values increase with an increasing minimum probability threshold, reflecting fewer false positives. The minimum probability threshold was selected as the value that equalized recall and precision.

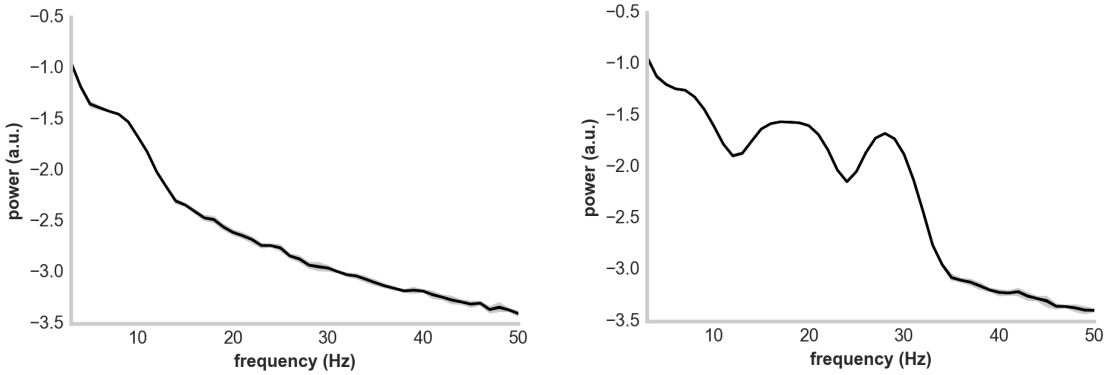

Figure 3.3 Synthetically generated power spectra. Synthetic power spectra were generated in order to compare human and algorithm performance to ground truth and to each other. Synthetic PSDs contained between 1 and 5 Gaussian peaks ranging from 6-30 Hz with 2 Hz fixed bandwidth and amplitude between 0.05 and 0.30. The spectral slope parameter ranged from -1 to -3 and additive white noise ranged between 0-0.4 standard deviations. Humans labeled the center frequencies of unprocessed PSDs (with 1/*f* component present). Left panel: 1 peak (8 Hz). Right panel: 5 peaks (6, 8, 16, 20, 28 Hz).

Simulating power spectra

We generated synthetic power spectra in order to validate the algorithm against ground truth knowledge of the number, center frequencies, and bandwidths of underlying oscillations. We define PSDs as consisting of a background spectrum with overlaid oscillatory components: $S = kN(f_c, \varsigma) + 1/f^{\chi} + B$, where the oscillations are characterized by the probability density function for a normal continuous random variable (N). The oscillatory component is shifted and scaled by the following parameters: amplitude (k), center frequency (f_c), and standard deviation (ς). The background spectrum obeys a power law characterized by its slope (χ). White noise (B) is added across all frequencies.

To generate a synthetic PSD with multiple peaks, oscillations are iteratively added to the background spectrum. Once all oscillations are included, white noise is added across all frequencies, creating a noisy set of synthetic PSDs (**Fig. 3.3**). Synthetic power spectra contained between 1 to 5 Gaussian peaks ranging from 6 to 30 Hz, with 2 Hz fixed bandwidth and amplitudes ranging between 0.05 and 0.30. The spectral slope parameter (χ) ranged from -1 to -3 and additive white noise ranged between 0.0 to 0.4 standard deviations.

Human labelers versus algorithm on synthetic power spectra

Human and algorithm performance were compared to the ground truth and to each other by labeling a noisy set of synthetic PSDs with multiple adjacent peaks. Labeling by independent expert human labelers ($N = 9$) was only done for the center frequencies of oscillations on the unprocessed PSDs (1/f component present). Precision and recall were calculated for both the algorithm and human labelers relative to the known parameters used to generate the synthetic power spectra. To be classified as a hit, the identified peak had to fall within a window set to twice the frequency resolution from the true peak (4 Hz window at 1 Hz resolution). If no peaks were found, accuracy, precision, and recall were all set to 0. Correct rejections were not included in performance estimates; had they been included, every non-peak that was correctly identified as such (most of the power spectra) would be marked as a correct rejection, skewing performance results.

Labeling electrophysiological power spectra

In addition to synthetic data, randomly selected EEG (N = 33) and LFP (N = 42) PSDs were also labeled by the algorithm and by human labelers. PSDs were calculated using Welch's method (1 second segments, 50% overlap, Hanning window). These PSDs were then fit and labeled from 5 to 50 Hz. The min_p parameter for the algorithm was set at 0.12 for EEG and 0.18 for LFP data. Accuracy measures were based on a round-robin scoring system, where one human labeler was designated as providing the "ground truth," and all other labelers were scored against this labeler. This process was iterated across all labelers such that on each run a different human labeler was designated as providing the ground truth. The algorithm did not provide ground truth in the round-robin scoring

system, but it was scored alongside human labelers for each round-robin iteration. Criteria for hits, misses, and accuracy precision were similar to those used for labeling synthetic power spectra specified above.

Individualized filtering of oscillatory components in EEG and LFP data
Oscillatory parameters were fit for each participant, block, and EEG/LFP channel separately**.** Filtering was done by multiplying the frequency domain representation of the raw data by a Gaussian with center frequency f_c and bandwidth ς. In scalp EEG analyses, for canonical alpha filtering, f_c = 10 Hz and ς = 2 Hz. For individualized filters, f_c and ς were determined on a per subject, channel, and block basis. If no alpha-proximal (6-14 Hz) peak was found by the algorithm, canonical band filtering was performed instead. If more than one peak was found, the mixture of Gaussians was summed and normalized to create a mixed-Gaussian filter (**see Fig. 3.5b**).

3.3 Results

Algorithm and human performance on synthetic power spectra
The algorithm was more sensitive than human labelers on synthetic, noisy power spectra with multiple peaks (**Fig. 3.4a,b**). The algorithm generated fewer false negatives than humans, so recall values were higher for the algorithm than for humans ($n_{algorithm}$ = 747, n_{humans} = 622; Mann-Whitney *U* test, p = 0.004). However, algorithm precision was lower than for human labelers (Mann-Whitney *U* test, $p < 10^{-36}$), suggesting that the algorithm was too sensitive and included more spurious peaks than human labelers. Recall decreased on average for both humans and the algorithm with increasing number of peaks, while precision was relatively more stable for both humans and the algorithm (**Fig. 3.4c,d**). That is, with more true peaks in the spectrum, both humans and the algorithm do not accordingly increase the number of peaks they identify. This may be driven by the difficulty in identifying two Gaussians that are closer to one another (see Fig. 4b for an example), though the effect of inter-peak difference in center frequencies on recall is modest (Mann-Whitney *U* test on differences > 8 Hz versus < 8 Hz, p = 0.044).

Algorithm and human performance on electrophysiological power spectra
Inter-rater reliability measures were used to determine if human-assigned labels on electrophysiological data were meaningful. Human labelers were consistent in peak labeling for both datasets (**Fig. 3.4d,e**), evidenced by recall above chance and precision with low variability in the round-robin scoring system (EEG: mean = 0.72, s.e.m = 0.01; LFP: mean = 0.64, s.e.m = 0.01). Note that when no peaks were found, recall and precision were set to zero, which penalized labelers for not finding any peaks and underestimated recall and precision (see **Methods**).

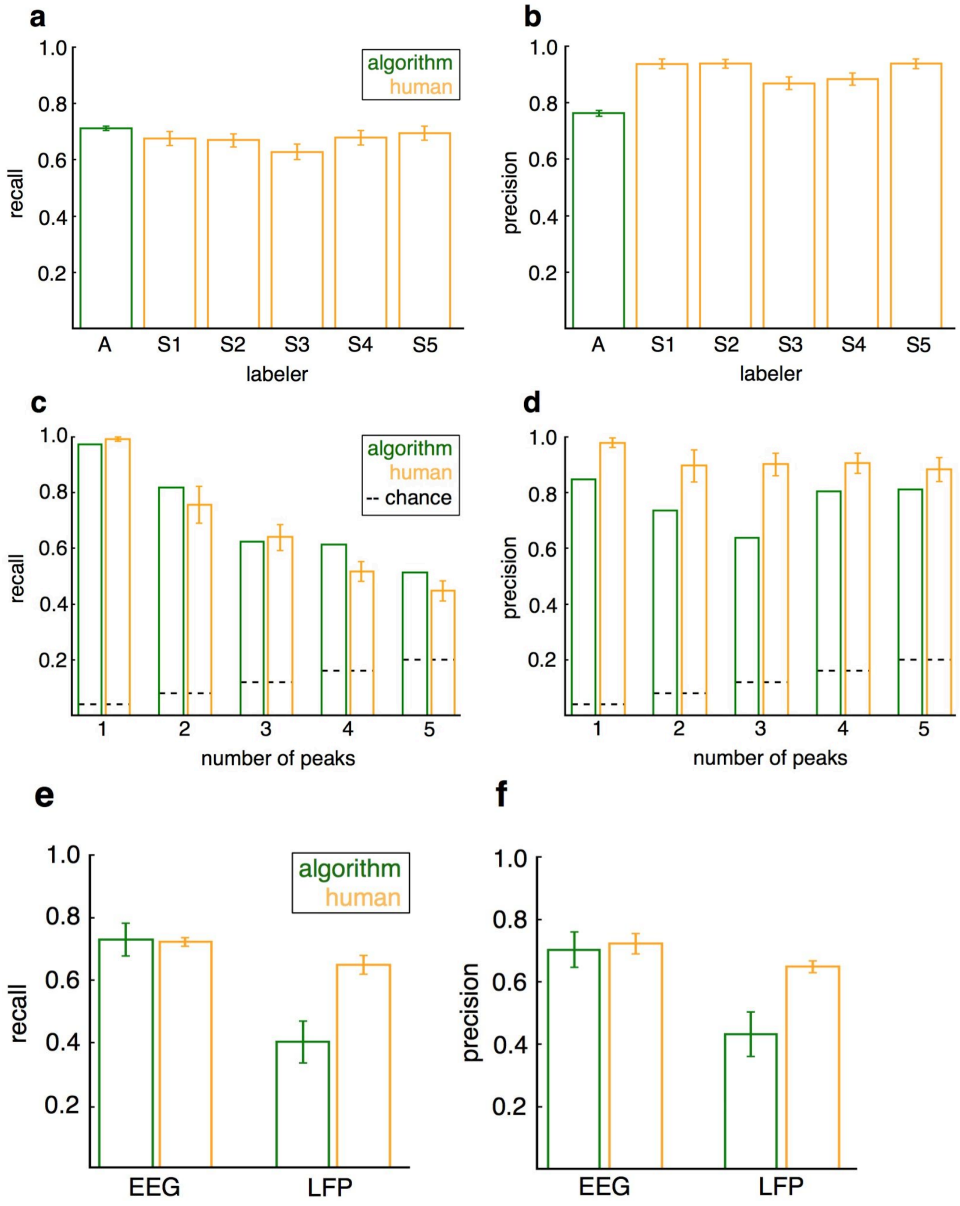

Figure 3.4 Algorithm performance compared to expert human raters. Recall (**a**) and precision (**b**) for the algorithm and each of the human labelers for synthetic data with multiple peaks. The algorithm is more sensitive than human labelers, generating (**a**) fewer false negatives, and (**b**) more false positives. (**c**) Recall for synthetic data decreases with increasing number of peaks for both the algorithm and human labelers, suggesting that more peaks are missed as the number of peaks increases. (**d**) Precision remains relatively stable across increasing number of peaks. (**e**) Recall and (**f**) precision for human and algorithm labels on EEG and LFP datasets. There was no significant difference in recall and precision between humans and the algorithm for EEG spectra, however the algorithm performs significantly worse than humans for LFP (yet still performs well above 0.2, the approximate level of chance performance).

Having determined that human-assigned labels were reliable, they were then used to estimate ground truth for each sample PSD. Precision and recall did not differ between the algorithm and humans for the EEG dataset ($n_{algorithm} = 33$, $n_{human} = 39$; Mann Whitney *U* test; recall: $p = 0.41$; precision: $p = 0.16$). Human labelers and the algorithm did not perform as well on the LFP dataset, with the algorithm performing significantly worse for both recall and precision ($n_{algorithm} = 42$, $n_{human} = 44$; recall: $p = 0.0002$; precision: $p = 0.006$). The poor performance on LFP data may be because the higher frequency oscillatory components in the LFP spectra were skewed and not Gaussian-shaped, thus violating GMM assumptions. We explicitly tested this by examining algorithm performance in the lower bands (< 16 Hz), where bandwidths were narrower and more Gaussian-shaped. In this range, the algorithm performs as well as humans (Mann Whitney *U* test; recall: $p = 0.29$; precision: $p = 0.18$). Although the algorithm did not perform as well as human labelers on the LFP dataset when including higher frequencies, it nevertheless performed well above chance (for 1 frequency peak chance is 0.04; for 5 frequency peaks chance performance is 0.2, as limited by the frequency range and resolution).

Cognitive significance of individualized oscillatory features

Scalp EEG

To demonstrate the generalizability of the oscillatory decomposition algorithm, we examined whether individualization of oscillatory parameters would improve the observed relationship between working memory and alpha band activity. We collected scalp EEG data from 11 participants performing a lateralized visual working memory task. Because visual tasks are strongly associated with event-related modulations in 8-12 Hz alpha amplitude over human visual cortex (Palva & Palva, 2007), we focused our analyses on this range. Specifically, during the late delay period, we expected an alpha increase as a function of memory load for difficult working memory tasks (Jensen, Gelfand, Kounios, & Lisman, 2002).

Across the 11 participants, 8 blocks, and 64 scalp EEG channels, we observed substantial heterogeneity in the distribution of alpha-proximal (6-14 Hz) oscillations (**Fig. 3.5a**) as compared to canonical alpha (8-12 Hz). We find that 20.6% of visual cortical channels showed no alpha-proximal oscillations while the vast majority, 70.7%, had one individualized alpha peak; a minority, 8.7%, showed two peaks, with no visual cortical channels showing more than two peaks. These algorithmically-identified center frequencies and bandwidths were used to construct individualized filters (**Fig. 3.5b,c**).

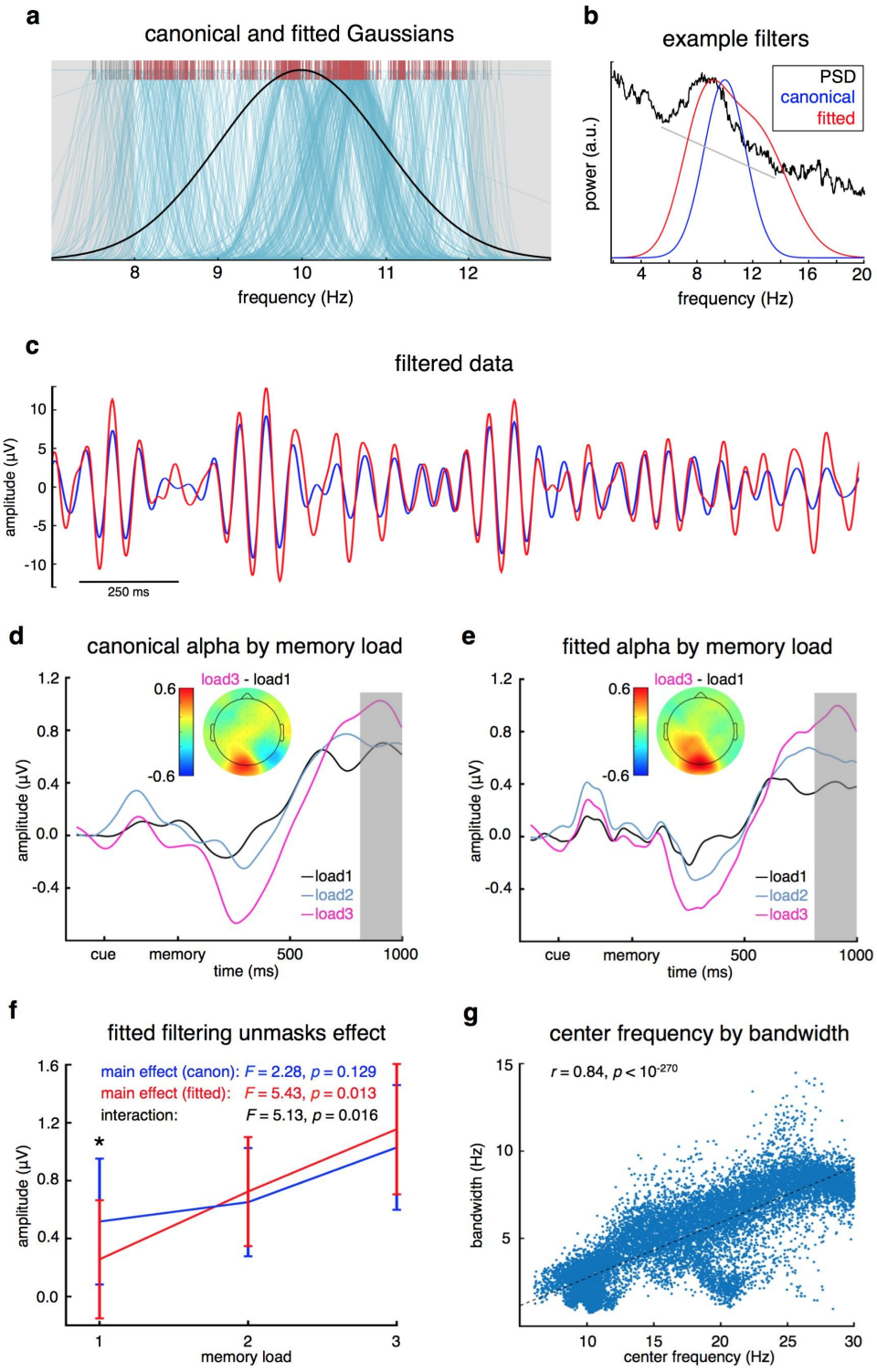

Figure 3.5 Working memory and oscillatory parameters for scalp EEG. (**a**) Many studies use canonical filters, such as 8-12 Hz alpha (black), that mask prevalent individual oscillatory differences (blue, center frequencies marked in red). Plotted are fitted Gaussians for all identified peaks in the human EEG data set. (**b**) Example of raw PSD, canonical 8-12 Hz filter (blue), and mixed Gaussian individualized filter (red, two Gaussians: f_c = 8.47,

$\varsigma = 1.61$; $f_c = 12.08$, $\varsigma = 2.35$) that give rise to (**c**) the bandpassed time domain signal (grey line below PSD highlights one large and one small oscillatory bump above background 1/*f*). Time course of (**d**) canonical filtered alpha and (**e**) fitted alpha across all 11 participants for each memory load (inset: scalp topography of average late alpha amplitude difference between load 3 and load 1; 800-1000 ms, grey box). (**f**) Using canonical alpha, there is no significant effect between average late alpha amplitude and load (blue, $p = 0.13$). A significant effect is unmasked when using individualized filters (red, $p = 0.013$), with a significant interaction between the two ($p = 0.016$; error bars, sem). (**g**) Bandwidth increases with higher frequencies.

To assess the utility of individualized filters, we compared event-related canonical and fitted alpha amplitudes over the visual cortex in the late processing window (800-1000 ms) (**Fig. 3.5d,e**). We find that canonical alpha amplitude contralateral to the hemifield of stimulus presentation did not scale with visual working memory load ($F_{2,20} = 2.28$, $p = 0.13$). In contrast, individually fitted alpha amplitude increased with visual working memory load ($F_{2,20} = 5.43$, $p = 0.013$). The difference between these two relationships was significant, such that there was a filter-method by memory load interaction ($F_{2,20} = 5.13$, $p = 0.016$) (**Fig. 3.5f**), with a *post hoc t*-test showing significant differences between the 1-item load condition ($p = 0.040$). Memory load explained nearly double the variance in fitted compared to canonical alpha (η^2: 35.2% versus 18.5%, respectively; all analyses used repeated measures ANOVA).

We observe that higher frequency oscillations have broader bandwidths ($r = 0.84$, $p < 10^{-270}$; **Fig. 3.5g**). This pattern is consistent across subjects, where *r* ranges from 0.74 to 0.94 ($p < 10^{-100}$ each). Intersubject differences across these two oscillatory parameters were distinct enough that subject identity could be inferred with 32.5% accuracy from those two parameters alone (*k*-nearest neighbors with 10-fold cross-validation; chance = 9.1% (1/11); $p < 10^{-100}$ based on permutation testing of using 1000 random permutations of subject identity relative to f_c and ς, where mean surrogate accuracy = 10.4%).

LFPs

To further establish the algorithm's utility and generalizability in the analysis of cognitive data, we compared our approach to results obtained using canonical frequency bands on previously published LFP data recorded from non-human primates performing a visual working memory task. In the initial report (Lara & Wallis, 2014), average oscillatory power was calculated during each temporal epoch using uniform bands of interest (1-7 Hz, 8-16 Hz, 20-35 Hz) across all channels. The authors reported band-specific differences in working memory precision as a function of high- or low-oscillatory power, with higher low frequency (< 16 Hz) and lower high frequency (20 - 35 Hz) power during a delay period associated with better precision. For the current analysis, power was instead calculated using algorithmically identified center frequencies (f_c) and bandwidths (ς) on a channel-by-channel basis, which yielded 431 total oscillations for subject *A* and 768 for

subject *B*. After removing cases where behavioral model fitting failed, final analyses were performed on 226 and 380 oscillation parameter/working memory precision pairs for each subject respectively. Rather than comparing the two methods directly – given that the previous result can be conceived of as pooling precision estimates by binning the individualized results – we instead sought to examine whether there was a more fine-grained relationship between oscillatory frequency and working memory precision, as hinted at by the prior findings.

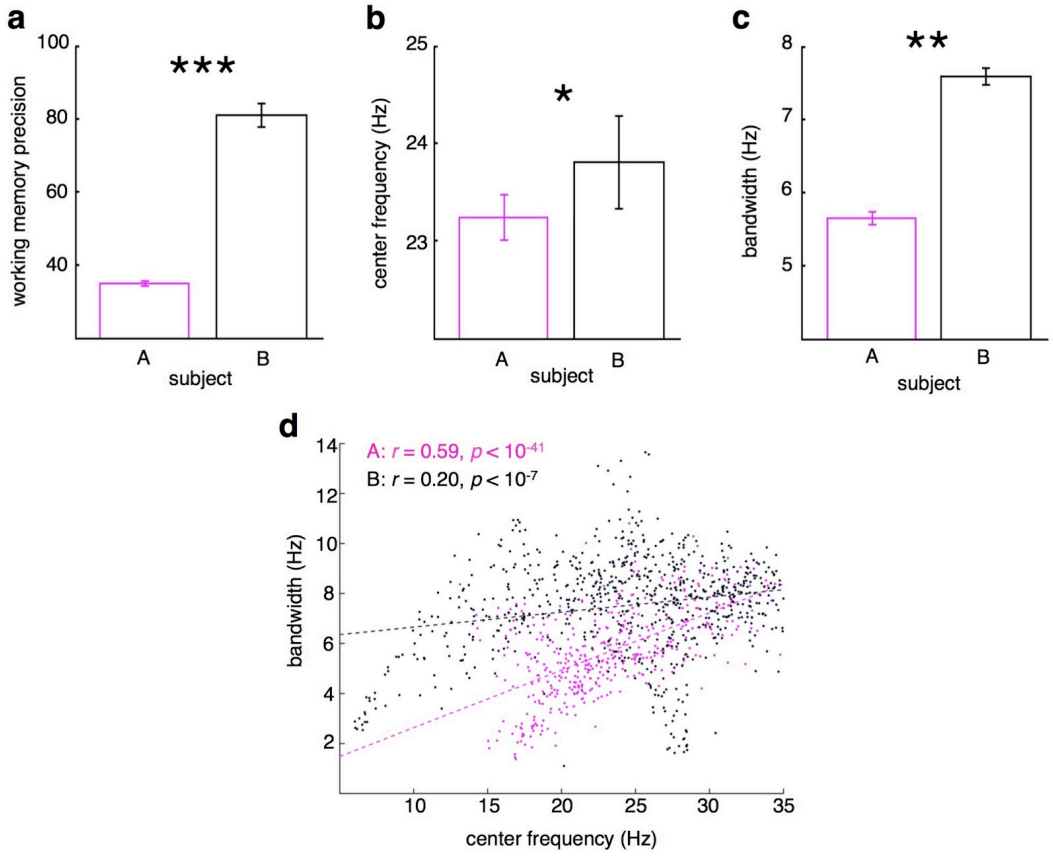

Figure 3.6 Working memory and oscillatory parameters in non-human primate LFPs. **(a)** There are significant working memory precision differences between subjects. Working memory precision was modeled using a variable precision model (see Ref. 14). These are associated with differences in the distribution of algorithmically identified oscillatory (**b**) center frequencies and (**c**) bandwidths. (**d**) As with the scalp EEG analysis, bandwidth increased as a function of center frequency in both subjects. (Error bars: s.e.m.; *$p = 0.0046$, **$p < 10^{-50}$, ***$p < 10^{-54}$)

Given the marked working memory precision (σ_{WM}) and oscillatory differences between the two subjects, we analyzed them separately. Compared to subject *B*, subject *A* had significantly lower delay period working memory precision (**Fig. 3.6a**; means (sem): 35.1 (0.7) and 81.2 (3.2) respectively; $p < 10^{-54}$), slower center frequencies (**Fig. 3.6b**; means (sem): 23.2 (0.2) and 24.2 (0.5) respectively; $p = 0.0046$), and narrower bandwidths (**Fig. 3.6c**; means (sem): 2.35 (0.02) and 2.71

(0.01); $p < 10^{-46}$) (two-sample *t*-tests, for all comparisons). Intersubject differences in center frequency and bandwidths of identified oscillations were so stark that subject identity could be inferred with 78.3% accuracy just using the two oscillatory parameters (*k*-nearest neighbors with 10-fold cross-validation; chance = 50%; $p < 10^{-100}$ based on permutation testing of using 1000 random permutations of subject identity relative to f_c and ς, where mean surrogate accuracy = 62.6%). Finally, similar to scalp the EEG data, we observed a significant relationship between the two oscillatory parameters for both subjects, such that faster oscillations had broader bandwidths (Fig. 4d; subject *A*, $r = 0.59$, $p < 10^{-41}$; subject *B*, $r = 0.20$, $p < 10^{-7}$; all comparisons Pearson correlations).

Given the working memory precision and oscillatory differences between subjects, we constructed a simple linear regression model to examine whether the precision of working memory information in the delay period could be predicted from a linear combination of oscillatory components ($\sigma_{WM} = \beta_0 f_c + \beta_1 \varsigma + \epsilon$) on an individual subject basis. This model was successful for both subjects (subject *A* ($N = 398$), $R^2 = 0.024$, $p = 0.0086$; subject *B* ($N = 277$), $R^2 = 0.046$, $p = 0.0016$). Another way to assess the impact of the oscillatory components on working memory precision is to examine the impact of removing the effect of the oscillatory components on between-subjects working memory precision differences. Subject identity accounts for 53.3% of the total precision variance; this drops significantly, to 47.2%, when the oscillatory parameters are partialled out (difference in correlations, $p = 0.029$).

3.4 Discussion

Here we present a novel method for algorithmically extracting oscillatory components in electrophysiological data and demonstrate that automatically extracted individualized oscillatory parameters predict performance on working memory tasks both in human EEG and non-human primate LFP data. We validated the algorithm on synthetic power spectra with predefined oscillatory and noise parameters. We found that it was able to correctly find all true peaks, but tended to overfit noise, identifying peaks where none existed. In other words, it had high recall (*i.e.*, sensitivity), but lower precision, whereas expert human raters had similar recall as, but higher precision than, the algorithm. We then compared the method to expert human labelers for both EEG and LFP power spectra. The algorithm performed as well as expert human labelers on EEG data and identified similar peaks. It performed significantly worse than human labelers on LFP data, possibly due to LFP oscillations failing to meet the assumptions of Gaussianity required by GMM, yet it still performed significantly above chance levels.

Previous reports that examine the functional relevance of center frequency often rely on peak-finding algorithms that simply search for a local maximum within the PSD across a predefined frequency range. Furthermore, as can be seen in the example in **Fig. 3.5b**, and as discovered from the synthetic spectra analyses,

multiple, possibly independent, overlapping oscillations often appear as one broadband bump atop the 1/*f* in the PSD. In these cases, peak-finding is a less optimal and more constrained solution than the method introduced here. Although the current algorithm tends to overfit oscillation center frequencies relative to human labelers, it offers the computational advantage of being a fast, automated approach that can be applied to large datasets, which are becoming more and more common across both scalp EEG and intracranial recordings across species.

By applying the algorithm to physiological data, we uncovered previously undescribed relationships between oscillatory center frequency and bandwidth. Across species, and for each individual, we found that faster oscillations have broader bandwidths, with individual differences in these parameters acting as "spectral fingerprints" allowing for the inference of subject identity in both humans and non-human primates. There is a rich literature showing that peak frequency slows between subjects with age (Obrist, 1954), with working memory maintenance (Cohen, 2011 ; Klimesch, 1999 ; Moran et al., 2010), and even within subjects over brief time periods where oscillatory frequency can speed up or slow down to optimize phase when the timing of an expected stimulus is known (Samaha et al., 2015 ; Samaha & Postle, 2015). However there are few studies examining the functional relevance of oscillatory bandwidth.

The observation that higher frequency oscillations have broader oscillatory bandwidths may relate to the underlying physiological generators of oscillations at different frequencies. For example, beta and gamma oscillations may have similar origins via local cortical excitatory-inhibitory (E-I) interactions while theta and alpha oscillations may be generated via larger thalamocortical network phenomena (Freyer et al., 2011 ; L. Wang et al., 2010). Driving fast-spiking inhibitory interneurons via optogenetic stimulation induces narrowband (< 5 Hz) oscillations in the gamma range (Cardin et al., 2009), with biophysical modeling of E-I subensembles showing similarly narrowband peaks (Börgers & Kopell, 2003 ; Brunel & Hakim, 1999 ; Wang & Buzsaki, 1996). LFP and EEG recordings capture many thousands of these subensembles, integrated across a relatively large spatial area. Thus, it may be that narrow beta/gamma bandwidths reflect fewer active subensembles. As more subensembles are recruited, the variance in the frequencies of these subensembles produces a broader apparent bandwidth in the LFP (if the center frequency variance across the active subensembles is unimodal) or even multiple apparent bands (if the center frequency variance is multimodal). An alternate, and not necessarily exclusive, interpretation comes from models of neural mass systems of beta/gamma oscillations, which predict that, for fixed E-I but variable drive/stimulation strength, bandwidth increases with frequency (Cohen, 2014). Thus, shifts in bandwidth might reflect changing inputs into the system rather than subensemble recruitment.

The current algorithm addresses often overlooked problems in cognitive and systems neuroscience. In particular, implicit reliance on canonical passbands can lead to both false positive and false negative results in analyses. For example, apparent group differences in power may be the results of shifts in center frequency of the oscillation and not changes in their respective power. This phenomenon can be illustrated by aging research. It is well accepted in the literature that alpha frequency slows with aging, yet there have also been reports of a decrease in alpha power with age (Obrist, 1954). If it is the case that younger adults have strong 10 Hz alpha center frequency while older adults have an equally high power alpha that has slowed to 8 Hz, canonical band analysis in the 8-12 Hz range will give the false appearance of older adults having lower alpha power relative to younger adults, as most of the oscillation range for older adults will be outside of the canonical alpha range. Additionally, changes in the 1/*f* background slope, seen with aging (Voytek, Kramer, et al., 2015b) and behavior (Podvalny et al., 2015), will shift narrowband power despite the fact that power in a narrowband oscillation has not changed relative to the background 1/*f* process (Voytek & Knight, 2015). In contrast, false negatives can also emerge, as demonstrated in our event-related EEG analyses, where canonical band analysis fails to capture the true underlying effect (**Fig 3.5**).

Finally, and perhaps more problematic, canonical band analyses commit researchers to tacit acceptance of predefined oscillatory bands having a functional role, rather than considering the underlying physiological mechanisms that may generate different spectral features with inter-individual differences. For example, recent advances in cross-frequency coupling analyses, such as phase-amplitude coupling, have provided a powerful means for probing mechanisms of neural communication (Voytek & Knight, 2015); however, these analyses typically generally rely on canonical bands, which is problematic given that phase-amplitude coupling is known to exhibit different phase coupling modes as a function of cortical region (Voytek, Canolty, et al., 2010a). With the algorithm introduced here, it may be possible to identify phase coupling modes across brain regions, task, and time, increasing specificity and accuracy of cross-frequency coupling analyses. Thus, the current method allows researchers to take full advantage of the rich variance present in oscillatory data, increases analytical power, and potentially provides greater insight into physiological mechanisms underlying oscillations.

Chapter 4

Concluding Remarks

The prefrontal cortex (PFC) holds a unique place in the hierarchy of cognitive processing. Unlike with damage to sensory cortices, PFC damage often does not produce obvious, well-defined sensory or motor deficits. Rather, patients with PFC lesions are often described as having fundamental changes to their character and behavior, leading researchers to attribute a higher-order regulatory function to this region. The PFC is domain-general, exerting control across virtually any complex behavior studied. Further, PFC influences processing in posterior regions independent of sensory modality. This goal of this thesis was to understand the spatiotemporal profile of domain-general cognitive control, centered in the PFC, and to examine the transformation of sensory information into concrete actions.

The first part of this thesis addresses a central question that has captivated scientists for over a century - how stimulus perception is translated into response selection. Based on results obtained using direct intracranial recordings from 16 participants completing 38 experimental sessions, we demonstrate that sustained high frequency neural activity centered in the PFC provides a domain general mechanism bridging perception and action. This activity predicts response time with near perfect accuracy, independent of stimulus and response modality. These results provide a foundational framework that explains how the brain connects stimulus processing with response execution.

The intracranial research provides clear evidence of a domain and modality general pattern of sustained neuronal activity that links sensory perception with behavioral output. This finding raises new questions about how this robust 'hand-off' between sustained and response systems is implemented. One intriguing hypothesis is that low frequency cortical dynamics serve as the mechanism of this interaction. For example, directional phase-amplitude coupling from sustained to response sites would reflect modulation of response execution by response selection processes. The time course of this coupling would provide insights as to the temporal profile of the relationship between response selection and execution. For example, does phase-amplitude coupling increase prior to the handoff, suggesting a peak in information transfer? Does this coupling change as a function of task demands, suggesting increased modulation for tasks requiring more cognitive control? Another critical question is whether phase-phase coupling in specific frequency bands segregates processing within the sustained and response networks, and whether this coupling changes prior to the handoff between systems. Understanding the mechanisms

underlying this handoff is critical for defining how the PFC influences processing in downstream regions.

The second part of this thesis introduces a novel method for analyzing electrophysiological data. Increasing evidence suggests that cognitive processing, including higher order control, is supported by oscillatory dynamics within local neuronal populations and across disparate brain regions. The PFC is proposed to exert domain general cognitive control via these oscillatory dynamics. To better understand the role of PFC in cognitive control, it is crucial to probe the frequency and bandwidths of these oscillations on an individual basis, unbiased by *a priori* assumptions and predefined frequency bands. However, the majority of research utilizes canonical frequency bands despite the widely reported variability in oscillatory frequencies across age, species, and cognitive state. Using our method we demonstrate the importance of this individual variability by relating individual differences in oscillatory bandwidth and frequency to working memory. The use of individualized frequency bands enabled us to probe relationships between task and behavior that were hidden by canonical band analyses.

This new approach yields numerous directions for future research, specifically for understanding the nature of neuronal communication within and between cortical networks. A critical question is whether the variability in center frequencies and bandwidths across the cortical mantle segregates networks. Are these networks coherent within themselves and how do they bias local information processing in higher frequency bands? Do center frequencies and bandwidths change based on task demands? Methodological questions also arise. For example, can the use of individualized frequency bands provide additional information about the role of PAC in behavior? Answering these questions will further the understanding of the physiological basis of cognitive control, and will bridge the results presented here, which focused on local neuronal processing in the HG band and response selection, with larger-scale cortical dynamics.

Chapter 5

References

Anderson, K. L., Rajagovindan, R., Ghacibeh, G. A., Meador, K. J., & Ding, M. (2010). Theta oscillations mediate interaction between prefrontal cortex and medial temporal lobe in human memory. *Cerebral Cortex*, *20*(7), 1604–1612. doi :10.1093/cercor/bhp223

Aron, A. R., Fletcher, P. C., Bullmore, E. T., Sahakian, B. J., & Robbins, T. W. (2003). Stop-signal inhibition disrupted by damage to right inferior frontal gyrus in humans. *Nature Neuroscience*, *6*(2), 115–116. doi :10.1038/nn1003

Aron, A. R., Robbins, T. W., & Poldrack, R. A. (2014). Inhibition and the right inferior frontal cortex: one decade on. *Trends in Cognitive Sciences*, *18*(4), 177–185. doi :10.1016/j.tics.2013.12.003

Azuar, C., Reyes, P., Slachevsky, A., Volle, E., Kinkingnehun, S., Kouneiher, F., et al. (2014). Testing the model of caudo-rostral organization of cognitive control in the human with frontal lesions. *Neuroimage*, *84*, 1053–1060. doi :10.1016/j.neuroimage.2013.09.031

Badre, D. (2008). Cognitive control, hierarchy, and the rostro–caudal organization of the frontal lobes. *Trends in Cognitive Sciences*, *12*(5), 193–200. doi :10.1016/j.tics.2008.02.004

Badre, D., & D'Esposito, M. (2009). Is the rostro-caudal axis of the frontal lobe hierarchical? *Nature Reviews Neuroscience*, *10*(9), 659–669. doi :10.1038/nrn2667

Badre, D., & Wagner, A. D. (2007). Left ventrolateral prefrontal cortex and the cognitive control of memory. *Neuropsychologia, 45*(13), 2883–2901. doi :10.1016/j.neuropsychologia.2007.06.015

Badre, D., Hoffman, J., Cooney, J. W., & D'Esposito, M. (2009). Hierarchical cognitive control deficits following damage to the human frontal lobe. *Nature Neuroscience*, *12*(4), 515–522. doi :10.1038/nn.2277

Barbey, A. K., Koenigs, M., & Grafman, J. (2013). Dorsolateral prefrontal contributions to human working memory. *Cortex*, *49*(5), 1195–1205. doi :10.1016/j.cortex.2012.05.022

Barceló, F., Suwazono, S., & Knight, R. T. (2000). Prefrontal modulation of visual processing in humans. *Nature Neuroscience*, *3*(4), 399–403. doi :10.1038/73975

Bari, A., & Robbins, T. W. (2013). Inhibition and impulsivity: Behavioral and neural basis of response control. *Progress in Neurobiology*, *108*, 44–79. doi :10.1016/j.pneurobio.2013.06.005

Benjamini, Y., & Hochberg, Y. (1995). Controlling the false discovery rate: a practical and powerful approach to multiple testing. *Journal of the Royal*

Statistical Society Series B, 57(1), 289-300. doi :10.2307/2346101
Bokil, H., Andrews, P., Kulkarni, J. E., Mehta, S., & Mitra, P. P. (2010). Chronux: A platform for analyzing neural signals. *Journal of Neuroscience Methods*, *192*(1), 146–151. doi :10.1016/j.jneumeth.2010.06.020
Börgers, C., & Kopell, N. (2003). Synchronization in networks of excitatory and inhibitory neurons with sparse, random connectivity. *Neural Computation*, *15*(3), 509–538. doi :10.1162/089976603321192059
Bradley, M. M., & Lang, P. J. (1999). *Affective norms for English words (ANEW): Instruction manual and affective ratings.* Technical Report C-1, The Center for Research in Psychophysiology, University of Florida.
Brunel, N., & Hakim, V. (1999). Fast global oscillations in networks of integrate-and-fire neurons with low firing rates. *Neural Computation*, *11*(7), 1621–1671. doi :10.1162/089976699300016179
Bruns, A. (2004). Fourier-, Hilbert- and wavelet-based signal analysis: are they really different approaches? *Journal of Neuroscience Methods*, *137*(2), 321–332. doi :10.1016/j.jneumeth.2004.03.002
Bullock, T. H. (1981). Neuroethology deserves more study of evoked responses. *Neuroscience*, *6*(7), 1203–1215.
Burke, J. F., Long, N. M., Zaghloul, K. A., Sharan, A. D., Sperling, M. R., & Kahana, M. J. (2014). Human intracranial high-frequency activity maps episodic memory formation in space and time. *Neuroimage*, *85*(P2), 834–843. doi :10.1016/j.neuroimage.2013.06.067
Burnham, K. P. (2004). Multimodel inference: understanding AIC and BIC in model selection. *Sociological Methods & Research*, *33*(2), 261–304. doi :10.1177/0049124104268644
Busch, N. A., Dubois, J., & Vanrullen, R. (2009). The phase of ongoing EEG oscillations predicts visual perception. *Journal of Neuroscience*, *29*(24), 7869–7876. doi :10.1523/jneurosci.0113-09.2009
Buzsaki, G., & Draguhn, A. (2004). Neuronal oscillations in cortical networks. *Science*, *304*(5679), 1926–1929. doi :10.1126/science.1099745
Buzsaki, G., Anastassiou, C. A., & Koch, C. (2012). The origin of extracellular fields and currents--EEG, ECoG, LFP and spikes. *Nature Reviews Neuroscience*, *13*(6), 407–420. doi :10.1038/nrn3241
Buzsaki, G., Logothetis, N., & Singer, W. (2013). Scaling brain size, keeping timing: evolutionary preservation of brain rhythms. *Neuron*, *80*(3), 751–764. doi :10.1016/j.neuron.2013.10.002
Callicott, J. H., Bertolino, A., Mattay, V. S., Langheim, F. J., Duyn, J., Coppola, R., et al. (2000). Physiological dysfunction of the dorsolateral prefrontal cortex in schizophrenia revisited. *Cerebral Cortex*, *10*(11), 1078–1092.
Canolty, R. T., & Knight, R. T. (2010). The functional role of cross-frequency coupling. *Trends in Cognitive Sciences*, *14*(11), 506–515. doi :10.1016/j.tics.2010.09.001
Canolty, R. T., Edwards, E., Dalal, S. S., Soltani, M., Nagarajan, S. S., Kirsch, H. E., et al. (2006). High gamma power is phase-locked to theta oscillations in human

neocortex. *Science*, *313*(5793), 1626–1628. doi :10.1126/science.1128115
Cardin, J. A., Carlén, M., Meletis, K., Knoblich, U., Zhang, F., Deisseroth, K., et al. (2009). Driving fast-spiking cells induces gamma rhythm and controls sensory responses. *Nature*, *459*(7247), 663–667. doi :10.1038/nature08002
Catani, M., Dell'acqua, F., Vergani, F., Malik, F., Hodge, H., Roy, P., et al. (2012). Short frontal lobe connections of the human brain. *Cortex*, *48*(2), 273–291. doi :10.1016/j.cortex.2011.12.001
Chao, L. L., & Knight, R. T. (1998). Contribution of human prefrontal cortex to delay performance. *Journal of Cognitive Neuroscience*, *10*(2), 167–177.
Cohen, D., & Halgren, E. (2009). Magnetoencephalography. Dans L. R. Squire, *Encyclopedia of Neuroscience*, (pp. 615–622). Oxford: Academic Press.
Cohen, M. X. (2011). Hippocampal-prefrontal connectivity predicts midfrontal oscillations and long-term memory performance. *Current Biology 21*(22), 1900–1905. doi :10.1016/j.cub.2011.09.036
Cohen, M. X. (2014). Fluctuations in oscillation frequency control spike timing and coordinate neural networks. *Journal of Neuroscience*, *34*(27), 8988–8998. doi :10.1523/JNEUROSCI.0261-14.2014
Cromer, J. A., Roy, J. E., & Miller, E. K. (2010). Representation of multiple, independent categories in the primate prefrontal cortex. *Neuron*, *66*(5), 796–807. doi :10.1016/j.neuron.2010.05.005
Crone, N. (1998). Functional mapping of human sensorimotor cortex with electrocorticographic spectral analysis. II. Event-related synchronization in the gamma band. *Brain*, *121*(12), 2301–2315. doi :10.1093/brain/121.12.2301
Curtis, C. E., & Lee, D. (2010). Beyond working memory: the role of persistent activity in decision making. *Trends in Cognitive Sciences*, *14*(5), 216–222. doi :10.1016/j.tics.2010.03.006
D'Esposito, M., & Postle, B. R. (2015). The cognitive neuroscience of working memory. *Annual Review of Psychology*, *66*, 115–142. doi :10.1146/annurev-psych-010814-015031
D'Esposito, M., Cooney, J. W., Gazzaley, A., Gibbs, S. E. B., & Postle, B. R. (2006). Is the prefrontal cortex necessary for delay task performance? Evidence from lesion and FMRI data. *Journal of the International Neuropsychological Society*, *12*(2), 248–260. doi :10.1017/S1355617706060322
Daffner, K. R., Mesulam, M. M., Holcomb, P. J., Calvo, V., Acar, D., Chabrerie, A., et al. (2000). Disruption of attention to novel events after frontal lobe injury in humans. *Journal of Neurology, Neurosurgery, and Psychiatry*, *68*(1), 18–24. doi :10.1136/jnnp.68.1.18
de Hemptinne, C., Swann, N. C., Ostrem, J. L., Ryapolova-Webb, E. S., San Luciano, M., Galifianakis, N. B., & starr, P. A. (2015). Therapeutic deep brain stimulation reduces cortical phase-amplitude coupling in Parkinson's disease. *Nature Neuroscience*, *18*(5), 779–786. doi :10.1038/nn.3997
Delorme, A., & Makeig, S. (2004). EEGLAB: an open source toolbox for analysis of single-trial EEG dynamics including independent component analysis. *Journal of Neuroscience Methods*, *134*(1), 9–21. doi :10.1016/j.jneumeth.2003.10.009

Diamond, A. (2002). Normal development of prefrontal cortex from birth to young adulthood: Cognitive functions, anatomy, and biochemistry. D. T. Stuss & R. T. Knight, *Principles of Frontal Lobe Function* (pp. 466–503). Oxford University Press. doi :10.1093/acprof:oso/9780195134971.003.0029

Duncan, J., & Owen, A. M. (2000). Common regions of the human frontal lobe recruited by diverse cognitive demands. *Trends in Neurosciences*, *23*(10), 475–483.

Duncan, J., Parr, A., Woolgar, A., Thompson, R., Bright, P., Cox, S., et al. (2008). Goal neglect and Spearman's g: competing parts of a complex task. *Journal of Experimental Psychology: General*, *137*(1), 131–148. doi :10.1037/0096-3445.137.1.131

Edwards, E., Nagarajan, S. S., Dalal, S. S., Canolty, R. T., Kirsch, H. E., Barbaro, N. M., & Knight, R. T. (2010). Spatiotemporal imaging of cortical activation during verb generation and picture naming. *Neuroimage*, *50*(1), 291–301. doi :10.1016/j.neuroimage.2009.12.035

Fedorenko, E., Duncan, J., & Kanwisher, N. (2012). Language-selective and domain-general regions lie side by side within Broca's area. *Current Biology*, *22*(21), 2059–2062. doi :10.1016/j.cub.2012.09.011

Fedorenko, E., Duncan, J., & Kanwisher, N. (2013). Broad domain generality in focal regions of frontal and parietal cortex. *Proceedings of the National Academy of Sciences*, *110*(41), 16616–16621. doi :10.1073/pnas.1315235110

Ferrier, D. (1878). The Goulstonian lectures on the localisation of cerebral disease. *British Medical Journal*, *1*(903), 555–559.

Fischler, M. A., & Bolles, R. C. (1981). Random sample consensus: a paradigm for model fitting with applications to image analysis and automated cartography. *Communications of the ACM*, *24*(6), 381–395. doi :10.1145/358669.358692

Flinker, A., Korzeniewska, A., Shestyuk, A. Y., Franaszczuk, P. J., Dronkers, N. F., Knight, R. T., & Crone, N. E. (2015). Redefining the role of Broca's area in speech. *Proceedings of the National Academy of Sciences*, *112*(9), 2871–2875. doi :10.1073/pnas.1414491112

Fonken, Y. M., Rieger, J. W., Tzvi, E., Crone, N. E., Chang, E., Parvizi, J., et al. (2016). Frontal and motor cortex contributions to response inhibition: evidence from electrocorticography. *Journal of Neurophysiology*, jn.00708.2015. doi :10.1152/jn.00708.2015

Freedman, D. J., & Assad, J. A. (2006). Experience-dependent representation of visual categories in parietal cortex. *Nature*, *443*(7107), 85–88. doi :10.1038/nature05078

Freedman, D. J., Riesenhuber, M., Poggio, T., & Miller, E. K. (2001). Categorical representation of visual stimuli in the primate prefrontal cortex. *Science*, *291*(5502), 312–316. doi :10.1126/science.291.5502.312

Freyer, F., Roberts, J. A., Becker, R., Robinson, P. A., Ritter, P., & Breakspear, M. (2011). Biophysical mechanisms of multistability in resting-state cortical rhythms. *Journal of Neuroscience*, *31*(17), 6353–6361. doi :10.1523/JNEUROSCI.6693-10.2011

Fries, P. (2005). A mechanism for cognitive dynamics: neuronal communication through neuronal coherence. *Trends in Cognitive Sciences*, *9*(10), 474–480. doi :10.1016/j.tics.2005.08.011

Fuster, J. M. (2002). Frontal lobe and cognitive development. *Journal of Neurocytology*, *31*(3-5), 373–385.

Fuster, J. M. (2015). *The Prefrontal Cortex*. Academic Press. doi :10.1016/b978-0-12-407815-4.00012-x

Fuster, J. M., Bodner, M., & Kroger, J. K. (2000). Cross-modal and cross-temporal association in neurons of frontal cortex. *Nature*, *405*(6784), 347–351. doi :10.1038/35012613

Haegens, S., Cousijn, H., Wallis, G., Harrison, P. J., & Nobre, A. C. (2014). Inter- and intra-individual variability in alpha peak frequency. *Neuroimage*, *92*, 46–55. doi :10.1016/j.neuroimage.2014.01.049

He, B. J. (2014). Scale-free brain activity: past, present, and future. *Trends in Cognitive Sciences*, *18*(9), 480–487. doi :10.1016/j.tics.2014.04.003

Heekeren, H. R., Marrett, S., Bandettini, P. A., & Ungerleider, L. G. (2004). A general mechanism for perceptual decision-making in the human brain. *Nature*, *431*(7010), 859–862. doi :10.1038/nature02966

Hermes, D., Miller, K. J., Vansteensel, M. J., Aarnoutse, E. J., Leijten, F. S. S., & Ramsey, N. F. (2011). Neurophysiologic correlates of fMRI in human motor cortex. *Human Brain Mapping*, *33*(7), 1689–1699. doi :10.1002/hbm.21314

Hernandez, A., Zainos, A., & Romo, R. (2002). Temporal evolution of a decision-making process in medial premotor cortex. *Neuron*, *33*(6), 959–972.

Jensen, O., Gelfand, J., Kounios, J., & Lisman, J. E. (2002). Oscillations in the alpha band (9–12 Hz) increase with memory load during retention in a short-term memory task. *Cerebral Cortex*, *12*(8), 877–882. doi :10.1093/cercor/12.8.877

Just, M. A., Cherkassky, V. L., Keller, T. A., & Minshew, N. J. (2004). Cortical activation and synchronization during sentence comprehension in high-functioning autism: evidence of underconnectivity. *Brain*, *127*(8), 1811–1821. doi :10.1093/brain/awh199

Kaiser, H. F. (1960). The application of electronic computers to factor analysis. *Educational and Psychological Measurement*, *20*(1), 141–151. doi :10.1177/001316446002000116

Kawahara, H., & Irino, T. (2005). Underlying principles of a high-quality speech manipulation system STRAIGHT and its application to speech segregation. In *Speech separation by humans and machines*, (pp. 167–180). Springer US. doi :10.1007/0-387-22794-6_11

Kayser, C., Montemurro, M. A., Logothetis, N. K., & Panzeri, S. (2009). Spike-phase coding boosts and stabilizes information carried by spatial and temporal spike patterns. *Neuron*, *61*(4), 597–608. doi :10.1016/j.neuron.2009.01.008

Khan, S., Gramfort, A., & Shetty, N. R. (2013). Local and long-range functional connectivity is reduced in concert in autism spectrum disorders. Proceedings of the National Academy of Science, *110*(8), 3107-3112. doi :10.1073/pnas.1214533110/

Kim, J. N., & Shadlen, M. N. (1999). Neural correlates of a decision in the dorsolateral prefrontal cortex of the macaque. *Nature Neuroscience*, *2*(2), 176–185. doi :10.1038/5739

Kishiyama, M. M., Yonelinas, A. P., & Knight, R. T. (2009). Novelty enhancements in memory are dependent on lateral prefrontal cortex. *Journal of Neuroscience*, *29*(25), 8114–8118. doi :10.1523/jneurosci.5507-08.2009

Klimesch, W. (1999). EEG alpha and theta oscillations reflect cognitive and memory performance: a review and analysis. *Brain Research Reviews*, *29*(2-3), 169–195.

Knight, R. T. (1984). Decreased response to novel stimuli after prefrontal lesions in man. *Electroencephalography and Clinical Neurophysiology*, *59*(1), 9–20.

Koechlin, E., Ody, C., & Kouneiher, F. (2003). The architecture of cognitive control in the human prefrontal cortex. *Science*, *302*(5648), 1181–1185. doi :10.1126/science.1088545

Kominek, J., & Black, A. W. (2004). The CMU Arctic speech databases. In *Fifth ISCA Workshop on Speech Synthesis*.

Krämer, U. M., Solbakk, A.-K., Funderud, I., Løvstad, M., Endestad, T., & Knight, R. T. (2013). The role of the lateral prefrontal cortex in inhibitory motor control. *Cortex*, *49*(3), 837–849. doi :10.1016/j.cortex.2012.05.003

Lachaux, J.-P., Axmacher, N., Mormann, F., Halgren, E., & Crone, N. E. (2012). High-frequency neural activity and human cognition: Past, present and possible future of intracranial EEG research. *Progress in Neurobiology*, *98*(3), 279–301. doi :10.1016/j.pneurobio.2012.06.008

Lara, A. H., & Wallis, J. D. (2014). Executive control processes underlying multi-item working memory. *Nature Neuroscience*, *17*(6), 876–883. doi :10.1038/nn.3702

Levy, B. J., & Wagner, A. D. (2011). Cognitive control and right ventrolateral prefrontal cortex: reflexive reorienting, motor inhibition, and action updating. *Annals of the New York Academy of Sciences*, *1224*(1), 40–62. doi :10.1111/j.1749-6632.2011.05958.x

Luck, S. J. (2014). *An introduction to the event-related potential technique*. Cambridge: MIT press. doi :10.1093/applin/amu028

Luria, A. R. (1973). *The Working Brain*. New York: Basic Books.

Manning, J. R., Jacobs, J., Fried, I., & Kahana, M. J. (2009). Broadband shifts in local field potential power spectra are correlated with single-neuron spiking in humans. *Journal of Neuroscience*, *29*(43), 13613–13620. doi :10.1523/JNEUROSCI.2041-09.2009

Mayberg, H. (2001). Depression and frontal-subcortical circuits: Focus on prefrontal-limbic interactions. J. L. Cummings & D. G. Lichter, *Frontal-subcortical circuits in psychiatric and neurological disorders* (pp. 177–206). New York: Guilford Press.

Miller, E. K., & Cohen, J. D. (2001). An integrative theory of prefrontal cortex function. *Annual Review of Neuroscience*, *24*, 167–202. doi :10.1146/annurev.neuro.24.1.167

Miller, K. J. (2010). Broadband spectral change: evidence for a macroscale correlate

of population firing rate? *Journal of Neuroscience*, *30*(19), 6477–6479. doi :10.1523/jneurosci.6401-09.2010
Miller, K. J., Hermes, D., Honey, C. J., Sharma, M., Rao, R. P. N., Nijs, den, M., et al. (2010). Dynamic modulation of local population activity by rhythm phase in human occipital cortex during a visual search task. *Frontiers in Human Neuroscience*, *4*, 197. doi :10.3389/fnhum.2010.00197
Miller, K. J., Honey, C. J., Hermes, D., Rao, R. P. N., denNijs, M., & Ojemann, J. G. (2014). Broadband changes in the cortical surface potential track activation of functionally diverse neuronal populations. *Neuroimage*, *85(2)*, 711–720. doi :10.1016/j.neuroimage.2013.08.070
Miller, K. J., Sorensen, L. B., & Ojemann, J. G. (2009). Power-law scaling in the brain surface electric potential. *PLoS Comput. Biol.*, *5(12)*. doi :10.1371/journal.pcbi.1000609.s001
Moran, R. J., Campo, P., Maestu, F., Reilly, R. B., Dolan, R. J., & Strange, B. A. (2010). Peak frequency in the theta and alpha bands correlates with human working memory capacity. *Frontiers in Human Neuroscience*, *4*, 200. doi :10.3389/fnhum.2010.00200
Mukamel, R., & Fried, I. (2012). Human intracranial recordings and cognitive neuroscience. *Annual Review of Psychology*, *63*, 511–537. doi :10.1146/annurev-psych-120709-145401
Mukamel, R., Gelbard, H., Arieli, A., Hasson, U., Fried, I., & Malach, R. (2005). Coupling between neuronal firing, field potentials, and FMRI in human auditory cortex. *Science*, *309*(5736), 951–954. doi :10.1126/science.1110913
Murray, J. D., Bernacchia, A., Freedman, D. J., Romo, R., Wallis, J. D., Cai, X., et al. (2014). A hierarchy of intrinsic timescales across primate cortex. *Nature Neuroscience*, *17*(12), 1661–1663. doi :10.1038/nn.3862
Nunez, P. L., & Srinivasan, R. (2006). *Electric Fields of the Brain: The Neurophysics of EEG*. Oxford University Press. doi :10.1093/acprof:oso/9780195050387.001.0001
Obrist, W. D. (1954). The electroencephalogram of normal aged adults. *Electroencephalography and Clinical Neurophysiology*, *6*, 235–244. doi :10.1016/0013-4694(54)90025-5
Ossandon, T., Vidal, J. R., Ciumas, C., Jerbi, K., Hamamé, C. M., Dalal, S. S., et al. (2012). Efficient "pop-out" visual search elicits sustained broadband γ activity in the dorsal attention network. *Journal of Neuroscience*, *32*(10), 3414–3421. doi :10.1523/JNEUROSCI.6048-11.2012
Palva, S., & Palva, J. M. (2007). New vistas for α-frequency band oscillations. *Trends in Neurosciences*, *30*(4), 150–158. doi :10.1016/j.tins.2007.02.001
Papademetris, X., Jackowski, M. P., Rajeevan, N., DiStasio, M., Okuda, H., Constable, R. T., & Staib, L. H. (2006). BioImage Suite: An integrated medical image analysis suite: An update. *The Insight Journal*, *2006*, 209.
Pedregosa, F., Varoquaux, G., & Gramfort, A. (2011). Scikit-learn: Machine learning in Python. *Journal of Machine Learning Research*. *12*, 2825-2830. doi :10.1007/978-1-4842-0958-5_8

Petrides, M. (2005). Lateral prefrontal cortex: architectonic and functional organization. *Philosophical Transactions of the Royal Society B: Biological Sciences*, *360*(1456), 781–795. doi :10.1126/science.1896849

Petrides, M., & Pandya, D. N. (2002). Association pathways of the prefrontal cortex and functional observations. D. T. Stuss & R. T. Knight, *Principles of Frontal Lobe Function*, *(*pp. 31–50). New York: Oxford University Press.

Podvalny, E., Noy, N., Harel, M., Bickel, S., Chechik, G., Schroeder, C. E., et al. (2015). A unifying principle underlying the extracellular field potential spectral responses in the human cortex. *Journal of Neurophysiology*, *114*(1), 505–519. doi :10.1152/jn.00943.2014

Preuss, T. M. (2011). The human brain: rewired and running hot. *Annals of the New York Academy of Sciences*, *1225*(S1), E182–E191. doi :10.1111/j.1749-6632.2011.06001.x

Race, E. A., Shanker, S., & Wagner, A. D. (2009). Neural priming in human frontal cortex: multiple forms of learning reduce demands on the prefrontal executive system. *Journal of Cognitive Neuroscience*, *21*(9), 1766–1781. doi :10.1162/jocn.2009.21132

Rainer, G., Rao, S. C., & Miller, E. K. (1999). Prospective coding for objects in primate prefrontal cortex. *Journal of Neuroscience*, *19*(13), 5493–5505.

Ray, S., & Maunsell, J. (2011). Different origins of gamma rhythm and high-gamma activity in macaque visual cortex. *PLoS Biol. 9*(4). doi :10.1371/journal.pbio.1000610.s008

Ray, S., Crone, N. E., Niebur, E., Franaszczuk, P. J., & Hsiao, S. S. (2008). Neural correlates of high-gamma oscillations (60-200 Hz) in macaque local field potentials and their potential implications in electrocorticography. *Journal of Neuroscience*, *28*(45), 11526–11536. doi :10.1523/jneurosci.2848-08.2008

Riès, S. K., Xie, K., Haaland, K. Y., Dronkers, N. F., & Knight, R. T. (2013). Role of the lateral prefrontal cortex in speech monitoring. *Frontiers in Human Neuroscience*, *7*, 703. doi :10.3389/fnhum.2013.00703

Roy, J. E., Riesenhuber, M., Poggio, T., & Miller, E. K. (2010). Prefrontal cortex activity during flexible categorization. *Journal of Neuroscience*, *30*(25), 8519–8528. doi :10.1523/JNEUROSCI.4837-09.2010

Ruscio, J., & Roche, B. (2012). Determining the number of factors to retain in an exploratory factor analysis using comparison data of known factorial structure. *Psychological Assessment*, *24*(2), 282–292. doi :10.1037/a0025697

Sadeh, B., Szczepanski, S. M., & Knight, R. T. (2013). Oscillations and behavior: the role of phase–amplitude coupling in cognition. G. R. Mangun, *Cognitive Electrophysiology of Attention*. Academic Press. doi :10.1016/b978-0-12-398451-7.00021-x

Sahin, N. T., Pinker, S., Cash, S. S., Schomer, D., & Halgren, E. (2009). Sequential processing of lexical, grammatical, and phonological information within Broca's area. *Science*, *326*(5951), 445–449. doi :10.1126/science.1174481

Samaha, J., & Postle, B. R. (2015). The speed of alpha-band oscillations predicts the temporal resolution of visual perception. *Current Biology, 25*(22), 2985–2990.

doi :10.1016/j.cub.2015.10.007
Samaha, J., Bauer, P., Cimaroli, S., & Postle, B. R. (2015). Top-down control of the phase of alpha-band oscillations as a mechanism for temporal prediction. *Proceedings of the National Academy of Sciences*, *112*(27), 8439–8444. doi :10.1073/pnas.1503686112
Schroeder, C. E., & Lakatos, P. (2009). Low-frequency neuronal oscillations as instruments of sensory selection. *Trends in Neurosciences*, *32*(1), 9–18. doi :10.1016/j.tins.2008.09.012
Schwarz, G. (1978). Estimating the dimension of a model. *The Annals of Statistics*, *6*(2), 461–464. doi :10.1214/aos/1176344136
Segrave, R. A., Thomson, R. H., Cooper, N. R., Croft, R. J., Sheppard, D. M., & Fitzgerald, P. B. (2010). Upper alpha activity during working memory processing reflects abnormal inhibition in major depression. *Journal of Affective Disorders*, *127*(1-3), 191–198. doi :10.1016/j.jad.2010.05.022
Siegel, M., Buschman, T. J., & Miller, E. K. (2015). Cortical information flow during flexible sensorimotor decisions. *Science*, *348*(6241), 1352–1355. doi :10.1126/science.aab0551
Siegel, M., Donner, T. H., & Engel, A. K. (2012). Spectral fingerprints of large-scale neuronal interactions. *Nature Reviews Neuroscience. 13*(2), 121-134. doi :10.1038/nrn3137
Sirota, A., Montgomery, S., Fujisawa, S., Isomura, Y., Zugaro, M., & Buzsaki, G. (2008). Entrainment of neocortical neurons and gamma oscillations by the hippocampal theta rhythm. *Neuron*, *60*(4), 683–697. doi :10.1016/j.neuron.2008.09.014
Sreenivasan, K. K., Curtis, C. E., & D'Esposito, M. (2014). Revisiting the role of persistent neural activity during working memory. *Trends in Cognitive Sciences*, *18*(2), 82–89. doi :10.1016/j.tics.2013.12.001
Stokes, M. G. (2015). 'Activity-silent' working memory in prefrontal cortex: a dynamic coding framework. *Trends in Cognitive Sciences*, *19*(7), 394–405. doi :10.1016/j.tics.2015.05.004
Stuss, D. T., & Knight, R. T. (2012). *Principles of Frontal Lobe Function*. New York: Oxford University Press.
Swann, N. C., Tandon, N., Pieters, T. A., & Aron, A. R. (2013). Intracranial electroencephalography reveals different temporal profiles for dorsal-and ventro-lateral prefrontal cortex in preparing to stop action. *Cerebral Cortex*, *23*(10), 2479–2488. doi :10.1093/cercor/bhs245
Szczepanski, S. M., & Knight, R. T. (2014). Insights into human behavior from lesions to the prefrontal cortex. *Neuron*, *83*(5), 1002–1018. doi :10.1016/j.neuron.2014.08.011
Szczepanski, S. M., Crone, N. E., & Kuperman, R. A. (2014). Dynamic changes in phase-amplitude coupling facilitate spatial attention control in fronto-parietal cortex. *PLoS Biol*. doi :10.1371/journal.pbio.1001936.s002
Toga, A. W., & Thompson, P. M. (2003). Mapping brain asymmetry. *Nature Reviews Neuroscience*, *4*(1), 37–48. doi :10.1038/nrn1009

Tottenham, N., Tanaka, J. W., Leon, A. C., McCarry, T., Nurse, M., Hare, T. A., et al. (2009). The NimStim set of facial expressions: Judgments from untrained research participants. *Psychiatry Research*, *168*(3), 242–249. doi :10.1016/j.psychres.2008.05.006

Uhlhaas, P. J., & Singer, W. (2010). Abnormal neural oscillations and synchrony in schizophrenia. *Nature Reviews Neuroscience*, *11*(2), 100–113. doi :10.1038/nrn2774

Vogel, E. K., & Machizawa, M. G. (2004). Neural activity predicts individual differences in visual working memory capacity. *Nature*, *428*(6984), 748–751. doi :10.1038/nature02447

Voytek, B., & Knight, R. T. (2010). Prefrontal cortex and basal ganglia contributions to visual working memory. *Proceedings of the National Academy of Sciences*. *107*(42), 18167-18172. doi :10.1073/pnas.1007277107/

Voytek, B., & Knight, R. T. (2015). Dynamic network communication as a unifying neural basis for cognition, development, aging, and disease. *Biological Psychiatry*, *77*(12), 1089–1097. doi :10.1016/j.biopsych.2015.04.016

Voytek, B., Canolty, R. T., Shestyuk, A., Crone, N. E., Parvizi, J., & Knight, R. T. (2010a). Shifts in gamma phase-amplitude coupling frequency from theta to alpha over posterior cortex during visual tasks. *Frontiers in Human Neuroscience*, *4*, 191. doi :10.3389/fnhum.2010.00191

Voytek, B., Davis, M., Yago, E., Barcelo, F., Vogel, E. K., & Knight, R. T. (2010b). Dynamic neuroplasticity after human prefrontal cortex damage. *Neuron*, *68*(3), 401–408. doi :10.1016/j.neuron.2010.09.018

Voytek, B., Kayser, A. S., Badre, D., Fegen, D., Chang, E. F., Crone, N. E., et al. (2015a). Oscillatory dynamics coordinating human frontal networks in support of goal maintenance. *Nature Neuroscience*, 1–10. doi :10.1038/nn.4071

Voytek, B., Kramer, M. A., Case, J., Lepage, K. Q., Tempesta, Z. R., Knight, R. T., & Gazzaley, A. (2015b). Age-related changes in 1/f neural electrophysiological noise. *Journal of Neuroscience*, *35*(38), 13257–13265. doi :10.1523/JNEUROSCI.2332-14.2015

Wallis, J. D., Anderson, K. C., & Miller, E. K. (2001). Single neurons in prefrontal cortex encode abstract rules. *Nature*, *411*(6840), 953–956. doi :10.1038/35082081

Wang, L., Yu, C., Chen, H., Qin, W., He, Y., Fan, F., et al. (2010). Dynamic functional reorganization of the motor execution network after stroke. *Brain*, *133*(4), 1224–1238. doi :10.1093/brain/awq043

Wang, X. J., & Buzsaki, G. (1996). Gamma oscillation by synaptic inhibition in a hippocampal interneuronal network model. *Journal of Neuroscience*, *16*(20), 6402–6413.

Wang, X.-J. (2010). Neurophysiological and computational principles of cortical rhythms in cognition. *Physiological Reviews*, *90*(3), 1195–1268. doi :10.1152/physrev.00035.2008

Watrous, A. J., Tandon, N., Conner, C. R., Pieters, T., & Ekstrom, A. D. (2013). Frequency-specific network connectivity increases underlie accurate spatiotemporal memory retrieval. *Nature Neuroscience*, *16*(3), 349–356.

doi :10.1038/nn.3315
Yarkoni, T., Poldrack, R. A., Nichols, T. E., Van Essen, D. C., & Wager, T. D. (2011). Large-scale automated synthesis of human functional neuroimaging data. *Nature Methods*, *8*(8), 665–670. doi :10.1038/nmeth.1635